

Coupled Dynamics of a Nanomechanical Resonator and Superconducting Quantum Circuits

Thesis by

Junho Suh

In Partial Fulfillment of the Requirements

for the Degree of

Doctor of Philosophy



California Institute of Technology

Pasadena, California

2011

(Defended March 9, 2011)

©2011

Junho Suh

All Rights Reserved

Dedicated to

my wife, Young-kyung and my daughter, Kahyun Claire

Acknowledgement

First, I would like to thank my advisor, Prof. Michael Roukes, for his continuous support on my graduate research. His advice guided me to the right path and his insights helped me see from a broader point of view.

I deeply appreciate Prof. Matt LaHaye's enormous help. The qubit experiments were done working as a team with him. He kindly taught me lots of detailed knowledge and gave me crucial guidance throughout the experiments.

Prof. Keith Schwab collaborated in all the experiments and directly supported the microwave resonator experiment. I appreciate all his help and support. His keen eye for details and view on the future of the field was always helpful.

I thank Dr. Matt Shaw for his help in the microwave resonator experiment. He was essential in designing and conducting the experiment, and his comments sharpened my understanding.

I would like to express my thanks to the Roukes group people — Igor Bargatin, Inna Kozinsky, Rassul Karabalin, Ron Lifshitz, Matt Matheny, Louis Guillermo, Ed Myers, Akshay Naik, Selim Hanay, Scott Kelber, Sotiris Masmanidis, Hongxing Tang, Jie Xiang, Philip Feng, and Sequoyah Aldridge — for helpful discussions and comments; Wonhee Lee, Blake Axelrod, and Ben Gudlewski for their time teaching me various fabrication tools; Derrick Chi and Xinchang Zhang for their help in device fabrication; Steve Stryker for his quality machining jobs; and Adam Sears for his help in the early stage of the work.

I also thank my Korean friends who kept my life enjoyable outside the lab — Youngshik Shin, Taewan Kim, Jihun Kim, Hyungjun Kim, Minseok Jang, Jaewon Song, Seokmin Jeon, Sonjong Hwang, and others.

Finally, I deeply thank my wife, Young-kyung Bae. This thesis could not have been finished without her support. I also thank my parents, grandmother, brother, and sister who have supported me throughout my life.

Abstract

The coupled dynamics of a nanomechanical resonator and superconducting quantum circuits are studied in three experiments, in the context of studying the quantum limit for force detection and quantum physics of macroscopic objects.

In the first experiment, the dispersive mechanical resonance shift from the interaction with a Cooper-pair box qubit is studied. The measured coupling strength is large enough to satisfy one of the conditions required to perform many of the proposed quantum nanomechanical measurements. The resonance shift also probes the microwave-driven response of the qubit, showing Rabi oscillation and Landau-Zener tunneling, proving the coherent dynamics of the qubit.

Second, the parametric excitation of nanomechanical motion is studied via experiments with a driven qubit. Degenerate parametric amplification and oscillation are demonstrated, with a new observation of nonlinear dissipation. The squeezing of the back-action noise from the detection amplifier is also observed, up to 4dB. It is the first demonstration using a qubit as an auxiliary system to modify the nanomechanical dynamics, showing a

possible route for generation of nanomechanical quantum states.

Finally, back-action cooling of nanomechanical motion has been investigated, which is implemented by capacitively coupling a high-Q coplanar waveguide microwave resonator to a nanomechanical resonator. The thermal state with 7.5 mechanical quanta on average is reached, a result that is ultimately limited due to increased bath heating with microwave power. The heating is consistent with a model based on two-level systems resonantly coupled to the nanomechanical mode. This additional heating suggests future efforts to improve coupling and for reducing two-level system density in materials employed to reach the motional ground state via back-action cooling.

Contents

Acknowledgement	iii
Abstract	v
List of figures	x
1 Introduction.....	1
2 Nanomechanical measurements of Cooper-pair box qubit.....	5
2.1 Theory	6
2.2 Sample fabrication.....	10
2.3 Experimental set-up.....	12
2.3.1 Measurement circuit.....	12
2.3.2 Capacitive detection of mechanical motion	13
2.4 Results	17
2.4.1 Dispersive shift of mechanical resonance	17
2.4.2 Periodicity in V_{cpb} and Φ	21
2.4.3 Correction for charge drift.....	26
2.4.4 Microwave spectroscopy of CPB.....	29
2.4.5 Landau-Zener tunneling of CPB with strong microwave excitation.....	37

2.5	Discussion	42
3	Parametric amplification and back-action noise squeezing by driven Cooper-pair box qubit	44
3.1	Parametric excitation of harmonic oscillator: amplification and noise squeezing	
	46	
3.2	Setup and results.....	48
3.2.1	Parametric amplification and oscillation.....	51
3.2.2	Nonlinear dissipation.....	52
3.2.3	Noise squeezing.....	56
3.3	Discussion.....	62
4	Cooling of a nanomechanical mode with a microwave resonator	65
4.1	Theory	67
4.1.1	Superconducting coplanar waveguide resonator	67
4.1.2	Back-action cooling of mechanical motion.....	68
4.2	Experimental Setup	71
4.2.1	Device parameters	71
4.2.2	Cryogenic circuit.....	71
4.2.3	Room temperature circuit.....	72

4.3	Results	74
4.3.1	Thermomechanical noise.....	74
4.3.2	Back-action cooling of mechanical motion.....	76
4.4	Discussion	83
5	Summary	84
Appendix A	Nuclear orientation thermometry.....	87
Appendix B	Mode shapes and resonance frequencies of a doubly-clamped beam.....	90
Appendix C	Coupled mode analysis of parametric amplification.....	91
Appendix D	Driven responses of nanomechanical resonator.....	93
Appendix E	Whispering gallery mode sapphire cavity filter for microwave phase noise reduction.....	95
	Bibliography.....	97

List of figures

Figure 1: Schematic of measurement circuit	16
Figure 2: Phase-locked loop circuit	17
Figure 3: Sample picture, measurement circuit, and measured dispersive shift of mechanical resonance	20
Figure 4: Dispersive shift vs. qubit control parameters	22
Figure 5: Periodicity in CPB gate charge and flux	25
Figure 6: Correction for CPB charge drift	28
Figure 7: Dispersive shift from weakly driven qubit	32
Figure 8: Qubit microwave resonance vs. gate charge	33
Figure 9: Qubit microwave resonance for different microwave frequencies.....	34
Figure 10: Estimate of qubit linewidth	36
Figure 11: Landau-Zener interference with strong qubit excitation	40
Figure 12: Scanning electron micrograph of the device and the measurement circuit diagram	50
Figure 13: Mechanical parametric amplification and oscillation by driven qubit	55
Figure 14: Nanomechanical resonance width vs. gate charge	56

Figure 15: Amplifier back-action noise squeezing	61
Figure 16: Displacement measurement noise floor estimate	62
Figure 17: Sample picture and measurement schematic.....	73
Figure 18: Thermomechanical noise power vs. bath temperature	75
Figure 19: CPW resonator loss due to two-level systems.....	78
Figure 20: Back-action cooling of mechanical motion.....	79
Figure 21: Heating rate from the two-level bath.....	81
Figure A1: Nuclear orientation thermometry.....	88
Figure D1: Driven response of nanomechanical resonator.....	94
Figure E1: Schematic of the filter circuit.....	96
Figure E2: Transmission through the filter circuit.....	96

Chapter 1

Introduction

Mechanical force sensors have been important experimental tools in physics, beginning with the torsional pendulums in Cavendish's experiment on the gravitational force¹ and Coulomb's works on the electrostatic force². Since then, modern day force sensors have provided improvements in sensitivity and versatility; among recent achievements are measurement of Coulomb forces down to a single electron³ and magnetic forces to a single spin⁴, attainment of atomic mass sensitivity⁵⁻⁷, and sensing gravitational waves⁸.

Even though these mechanical sensors are macroscopic in size and their dynamics can be described well by classical mechanics, their ultimate force sensitivity is limited by the position uncertainty given by quantum mechanics — the so-called “standard quantum limit” ($x_{SQL} = \sqrt{\hbar/2m\omega}$) for a harmonic oscillator⁹. This is an interesting region where classical mechanics meets the uncertainty principle on the macroscopic scale. The standard quantum limit means that the limit of detection for measuring a classical force with a harmonic oscillator, if all thermal sources of fluctuation are reduced, will be set by

the uncertainty principle for position of the harmonic oscillator. This connection between two physical regimes was the starting point of my graduate research and I aimed to observe signatures of quantum physics at the sub-micron scale, using miniature mechanical sensors — nanomechanical resonators.

Recent advances in nanotechnology have enabled the fabrication of tiny mechanical resonators, which vibrate fast enough that the quantum energy is comparable to the thermal energy at millikelvin temperatures^{10, 11}. In this regime, close to quantum ground states, a resonator is expected to show the properties of a quantum harmonic oscillator, for example, energy quantization and quantum jumps¹² between energy states. The actual magnitude of nanomechanical motion near the quantum ground state is very tiny — only on the order of femto meters. To detect this minute motion, cryogenic detectors such as single-electron transistors¹³⁻¹⁵, atomic point contacts¹⁶, and quantum point contacts¹⁷ have been developed. It turns out that quantum physics also dictates the condition for an ideal measurement and we must consider the quantum back-action of measurement to detect, but not destroy, quantum states¹⁸. Such observations are known as quantum non-demolition (QND) measurements. Superconducting quantum circuits, such as Josephson-junction qubits¹⁹⁻²¹ and low-loss microwave resonators²² are good candidates for this

purpose, since they can generate the nonlinear coupling needed for QND and operate well in a cryogenic environment²³⁻²⁵. In this context, I set my experimental goal as obtaining measurements of the dynamics of a nanomechanical resonator coupled to a superconducting quantum circuit.

In the first two of my experiments, the coupled dynamics of a nanomechanical resonator and a superconducting Cooper-pair box qubit are studied. The interaction results in a mechanical resonance shift that is dependent on the qubit state. This is used to probe the stationary and driven dynamics of the qubit such as Rabi-oscillation and Landau-Zener tunneling. The resonance shift, in turn, also affects the dynamics of the nanomechanical resonator, and parametric amplification and oscillation of mechanical motion are observed. Due to the phase-sensitive nature of the amplification process, the back-action noise from the detection amplifier is reduced in only one phase relative to the qubit excitation, this provides a demonstration of noise squeezing.

In the last experiment, a superconducting microwave resonator is employed as the detector of nanomechanical motion. The microwave photons also apply a force to the nanomechanical resonator, and the phase lag in the back-action force reduces the thermal

motion of the mechanical resonator. The observed cooling is from 140 to 7.5 mechanical quanta. Heating against the back-action cooling is also identified, and it is consistent with a resonant coupling of a hot two-level system bath to the mechanical mode.

The coupled dynamics demonstrated in this work show first steps toward achievement of mechanical quantum states. To achieve the goal of generating and controlling mechanical quantum states in the future, the quality of the mechanical resonator and the quantum circuit elements requires improvements, and different implementations to provide better coupling might have to be considered. These efforts could also lead us to reach the quantum limit of force sensing, to reveal the physics at the boundary between the classical and quantum regimes.

Chapter 2

Nanomechanical measurements of Cooper-pair box qubit

Preparation and measurement of macroscopic mechanical quantum states is of considerable interest. The approach of coupling superconducting qubits to nanoelectromechanical systems (NEMS) has received recent theoretical attention^{23, 26-38}.

In this work, we experimentally demonstrated such a coupled system. This coupling results in a dispersive shift of the nanomechanical frequency that is the mechanical analogue of the “single-atom index effect”³⁹ in cavity quantum electrodynamics (CQED) experiments. The large magnitude of the dispersive interaction has enabled NEMS-based spectroscopy of the CPB, and permits observation of Landau-Zener (LZ) interference effects. These efforts constitute the first demonstration of coupling between a macroscopic mechanical system and a fully coherent quantum process.ⁱ

ⁱ After this work is published, a similar approach with a phase qubit read-out demonstrated the mechanical ground state and the observation of a few number states.¹¹

2.1 Theory

The nanomechanical resonator employed in this work uses the fundamental mode, in-plane flexural resonance of a suspended silicon nitride nanostructure. This mode can be reasonably well-described as a damped harmonic oscillator. Similar to the case for an electromagnetic oscillator, a Hamiltonian operator for the nanoresonator can be written in terms of creation \hat{a}^\dagger and annihilation \hat{a} operators, resulting in $\hat{H}_{NR} = \hbar\omega_{NR}(a^\dagger a + \frac{1}{2})$, where \hbar is Planck's constant and the quanta $N = \langle a^\dagger a \rangle$ in the mode are now mechanical quanta.

A split-junction CPB qubit,¹⁹ formed by two Josephson tunnel junctions and a superconducting Al loop, is coupled to the nanoresonator through capacitance, C_{NR} (Fig.

3). The CPB can be described by a simple spin-1/2 Hamiltonian⁴⁰

$$\hat{H}_{CPB} = \frac{E_{el}}{2} \hat{\sigma}_z - \frac{E_J}{2} \hat{\sigma}_x, \text{ where } \hat{\sigma}_z \text{ and } \hat{\sigma}_x \text{ are Pauli matrices in the CPB's charge basis.}$$

The first term in \hat{H}_{CPB} is the electrostatic energy difference

$$E_{el} = 8E_C(n_{cpb} + n_{NR} - n - \frac{1}{2}) \text{ between the } n \text{ and } n+1 \text{ charge states with the charging}$$

energy $E_C = \frac{e^2}{2C_\Sigma}$ determined by the CPB island's total capacitance

$C_\Sigma = C_{NR} + C_{cpb} + 2C_J$, where C_J is the capacitance of each Josephson junction. Here

$$n_{cpb} = \frac{C_{cpb}V_{cpb}}{2e} \text{ and } n_{NR} = \frac{C_{NR}V_{NR}}{2e} \text{ are supplied through the capacitances } C_{cpb} \text{ and}$$

C_{NR} to an independent gate electrode and the nanoresonator, which are held at potentials V_{cpb} and V_{NR} , respectively (Fig. 3b). The second term in \hat{H}_{CPB} is the Josephson energy of the junctions $E_J = E_{J0} \left| \cos\left(\frac{\Phi}{\Phi_0} \pi\right) \right|$, where Φ is the externally applied magnetic flux and $\Phi_0 = \frac{h}{2e}$ is the flux quantum. From the diagonalization of \hat{H}_{CPB} ,¹⁹ one finds the CPB ground state $|-\rangle$ and excited state $|+\rangle$ to be separated by the transition energy $\Delta E = \sqrt{E_{el}^2 + E_J^2}$.

Displacement x of the nanoresonator results in linear modulation of the capacitance between the nanoresonator and CPB, $C_{NR}(x) \approx C_{NR}(0) - \frac{\partial C_{NR}}{\partial x} x$, which modulates the electrostatic energy of the CPB through n_{NR} and E_C . This results in the interaction Hamiltonian $\hat{H}_{int} = \hbar \lambda (a^\dagger + a) \hat{\sigma}_z$ where

$$\lambda \approx -4n_{NR} \frac{E_C}{\hbar} \frac{x_{zp}}{d} \quad (\text{Eq. 1})$$

is the capacitive coupling constant, $x_{zp} = \sqrt{\frac{\hbar}{2m\omega_{NR}}}$ is the nanoresonator's zero-point deviation, and $d \sim 300$ nm is the separation between the CPB and NEMS. For parameters demonstrated in this work, $\left| \frac{\lambda}{2\pi} \right| \sim 0.5 - 3$ MHz.

The formal connection to CQED becomes clear when the full system Hamiltonian

$\hat{H} = \hat{H}_{NR} + \hat{H}_{CPB} + \hat{H}_{int}$ is transformed to the energy eigenbasis of the qubit

$$\hat{H} = \hbar\omega_{NR}a^\dagger a + \frac{\Delta E}{2}\hat{\sigma}_z + \hbar\lambda(a^\dagger + a)\left(\frac{E_{el}}{\Delta E}\hat{\sigma}_z - \frac{E_J}{\Delta E}\hat{\sigma}_x\right) \quad (\text{Eq. 2})$$

where $\hat{\sigma}_z$ and $\hat{\sigma}_x$ are now Pauli matrices in the CPB's energy basis. Eq. 2 is similar to a Jaynes-Cummings-type Hamiltonian.⁴¹ With the qubit and nanoresonator far-detuned (i.e., $\hbar|\lambda|\sqrt{N} \ll |\Delta E - \hbar\omega_{NR}|$), the dispersive coupling limit is realized and, to lowest order, the system undergoes a shift in energy that can be viewed as a CPB-dressed correction to the nanoresonator's frequency²³

$$\frac{\Delta\omega_{NR}}{2\pi} = \frac{\hbar\lambda^2}{\pi} \frac{E_J^2}{\Delta E(\Delta E^2 - (\hbar\omega_{NR})^2)} \langle \hat{\sigma}_z \rangle \quad (\text{Eq. 3}).$$

For fixed E_J , $\frac{\Delta\omega_{NR}}{2\pi}$ is greatest at CPB charge degeneracy points, where $E_{el} = 0$. Because $\Delta E > \hbar\omega_{NR}$, $\frac{\Delta\omega_{NR}}{2\pi} < 0$ when the CPB resides in the ground state ($\langle \hat{\sigma}_z \rangle = -1$) and $\frac{\Delta\omega_{NR}}{2\pi} > 0$ when the CPB fully occupies the excited state ($\langle \hat{\sigma}_z \rangle = 1$). In close analogy to the single-atom refractive shift³⁹ that arises in dispersive CQED, this can be interpreted as the CPB providing a state-dependent polarizability or quantum capacitance⁴²⁻⁴⁴ that electrostatically “pulls” the nanoresonator's frequency.

The spin-1/2 approximation for the CPB Hamiltonian reproduces the main features of coupled dynamics, but needs to be corrected when the qubit is biased away from a charge

degeneracy point. To model the dispersive frequency shift $\Delta\omega_{NR}/(2\pi)$ of the nanoresonator over the full range of gate voltages V_{cpb} used in the experiment, the full expressions for the CPB⁴⁰ and interaction Hamiltonians are employed, given, respectively, by

$$\hat{H}_{CPB} = \sum_n \left\{ 4E_C (n - n_{cpb} - n_{NR})^2 |n\rangle\langle n| - \frac{E_J}{2} (|n+1\rangle\langle n| + |n\rangle\langle n+1|) \right\} \quad (\text{Eq. 4})$$

and

$$\hat{H}_{\text{int}} = - \sum_n 2\lambda\hbar (n - n_{cpb} - n_{NR}) (\hat{a} + \hat{a}^\dagger) |n\rangle\langle n|.$$

To account for contributions from charge states other than n and $n+1$, 11 adjacent charge states are included in the calculation. The eigenstates of the uncoupled Hamiltonian $\hat{H} = \hat{H}_{CPB} + \hat{H}_{NR}$ are calculated numerically first as a function of a V_{cpb} and Φ . The correction to the energy levels due to \hat{H}_{int} and hence the dispersive shift of the nanoresonator $\Delta\omega_{NR}/(2\pi)$ are then calculated using second-order time-independent perturbation theory. It is important to note, that in the vicinity of a charge degeneracy point, $0.25 \leq n_{CPB} \leq 0.75$, use of the full CPB Hamiltonian results in less than 5% correction to $\Delta\omega_{NR}/(2\pi)$ calculated from spin-1/2 model. At degeneracy the correction is less than 1%.

2.2 Sample fabrication

The substrate is composed of a 100-nm-thick low-stress SiN layer on top of a Si wafer. The Cooper Pair Box (CPB) is patterned using electron-beam lithography and double-angle evaporation of aluminum⁴⁵. The thickness of the island and the ground leads are ~ 60 nm and ~ 20 nm, respectively. The island is coupled to the ground leads via two small ($\sim 100 \times 100$ nm²) Al/AlO_x/Al Josephson tunnel junctions, and is arranged in a DC-SQUID configuration. Dr. Pierre Echternach and R.E. Muller conducted the e-beam lithography and the qubit fabrication.

The aluminum layer used to define the nanoresonator, and which ultimately serves as the electrode on top of the nanoresonator, is patterned in the same step as the CPB. This layer acts as an etch mask for undercutting the nanoresonator. To protect the CPB during etching, a layer of PMMA is spun on the sample, and a small window defining the nanoresonator is opened using a second e-beam lithography step. The nanoresonator is then undercut in an ECR etcher with Ar/NF₃ plasma: The first step is an anisotropic SiN etch that defines the resonator beam, and the second is an isotropic etch of the underlying Si to undercut the beam.

The sample parameters are,

$\omega_{NR}/2\pi = 58$ MHz	Nanoresonator fundamental in-plane resonance frequency
$K \sim 60$ N/m	Nanoresonator effective spring constant given by $K = \alpha M_{geom} \omega_{NR}^2$, where $M_{geom} \approx 9 \times 10^{-16}$ kg is the estimated geometrical mass and $\alpha=0.48$ is found by assuming that the CPB couples to the average displacement of the nanoresonator over the length of the CPB island
$Q = 30,000\text{--}60,000$	Typical nanoresonator quality factor for the range of temperatures and actuation/detection voltages V_{GNR} used
$E_C/h = 13\text{--}15$ GHz	Estimated CPB charging energy from spectroscopy (lower bound) and LZ measurements (upper bound)
$E_{J0}/h \sim 13$ GHz	Estimated CPB maximum Josephson energy from spectroscopy
$C_{NR} = 43$ aF	Measured nanoresonator-to-CPB capacitance
$d \sim 300$ nm	Resonator/CPB spacing
$\partial C_{NR} / \partial x \sim 40\text{--}50$ pF/m	Derivative of resonator/CPB capacitance estimated from finite element simulation
$C_{cpb} = 17$ aF	Measured CPB gate capacitance
$\lambda/(2\pi) \sim 0.5\text{--}3$ MHz	Coupling strength calculated using $\Delta\omega_{NR}/(2\pi)$ data, assuming $E_J/h=12$ GHz, for $V_{NR} = 2\text{--}15$ V

2.3 Experimental set-up

2.3.1 Measurement circuit

The measurement is done on a dilution refrigerator located inside of a RF-shielded room. (Fig. 1) Four DC lines are used: V_{cpb} for biasing the CPB; V_{NR} for controlling the coupling between the CPB and nanoresonator; V_{GNR} for controlling the coupling between the nanoresonator and detection circuit; and V_{flux} for biasing a homemade current source to energize the solenoid for application of flux Φ to the CPB. V_{cpb} and V_{flux} are supplied by a DAC card and routed into the shielded room using optical isolators. V_{NR} and V_{GNR} are supplied by batteries located in the shielded room. V_{cpb} , V_{NR} , and V_{GNR} are filtered at room temperature (RT) at the input to the dilution refrigerator using commercial Pi-filters and Cu powder filters.⁴⁶ From RT to the mixing chamber (MC), these lines are each composed of ~ 2 meters of lossy stainless steel coax, with two stages of Cu powder filters (at 1 K and MC). The typical total attenuation from RT to the MC is estimated to be about -100dB at 10 GHz.

High frequency lines providing radio frequency excitation V_{RF} of the nanoresonator and microwave excitation V_{μ} of the CPB are routed into the shielded room through DC blocks and into the dilution refrigerator via commercial high-pass filters and attenuators. They

are attenuated and thermalized at 1 K using cryogenic-compatible attenuators. At 1K, V_{RF} is fed into the coupled port (-20 dB) of a directional coupler for the reflectometry measurements. The output port of the directional coupler feeds V_{RF} to the actuation gate electrode of the nanoresonator for excitation. And the input port of the directional coupler feeds the reflected component V_r through a Miteq AFS-series cryogenic amplifier to the room-temperature electronics that compose the phase-lock loop (Fig. 2). Bias-tees anchored to the MC are used to combine V_μ and V_{RF} with V_{cpb} and V_{GNR} , respectively. To provide additional filtering between the MC and the sample stage, all lines are fed through lossy stainless steel coax.

2.3.2 Capacitive detection of mechanical motion

For this work, capacitive displacement transduction scheme is employed. Radio frequency reflectometry is used to measure the nanomechanical frequency shift $\Delta\omega_{NR} / (2\pi)$ ⁴⁷. A DC potential difference $\Delta V = V_{GNR} - V_{NR}$ is applied across the capacitor C_{GNR} , coupling the nanoresonator's motion to the charge on the actuation-detection electrode. Upon application of $V_{RF}(\omega)$ to the electrode, the response of the coupled nanoresonator-electrode system can be modeled as a series RLC circuit with impedance⁴⁷ $Z_{NR}(\omega) = jL_{NR}(\omega^2 - \omega_{NR}^2) / \omega + R_{NR}$. Here $R_{NR} \approx Kd_{GNR}^2 / (\omega_{NR} Q C_{GNR}^2 \Delta V^2)$

and $L_{NR} = QR_{NR} / \omega_{NR}$, where $d_{GNR} \sim 100$ nm is the spacing between the nanoresonator and electrode. For typical values of coupling voltage used in our experiment, $\Delta V \sim 5\text{--}10$ V, $R_{NR} \sim 0.5\text{--}2$ M $\Omega \gg Z_0$, where $Z_0 = 40$ Ω is the characteristic impedance of the transmission line feeding the actuation-detection electrode.

To overcome the impedance mismatch, we use an LC network to transform $Z_{NR}(\omega_{NR})$ closer to Z_0 . The LC network is formed by a commercial, copper-wound coil ($L_T \approx 5.6$ μH) and the stray capacitance ($C_T \sim 1.0$ pF) of the PC board upon which the sample sits. The components are chosen so that $\omega_{LC} = \sqrt{1/(L_T C_T)} \approx \omega_{NR}$. Thus when the RF drive frequency is tuned into resonance with the nanoresonator and LC circuit, $\omega = \omega_{NR} = \omega_{LC}$, the total impedance seen looking from the transmission line into the impedance matching network is given by $Z(\omega_{NR}) = L_T / (C_T R_{NR})$, where it is assumed for simplicity that the matching network is lossless. For our parameters, $Z(\omega_{NR}) \sim 2\text{--}10$ Ω .

For perfect matching to the transmission line, $Z(\omega_{NR}) = Z_0$, the reflection coefficient $\Gamma = (Z(\omega_{NR}) - Z_0) / (Z(\omega_{NR}) + Z_0) = 0$. A small change in the nanoresonator's frequency $\Delta\omega_{NR} / (2\pi)$ leads to a correction given by $\Delta\Gamma \approx jQ\Delta\omega_{NR} / \omega_{NR}$. Thus a shift in the

nanomechanical frequency $\Delta\omega_{NR}/(2\pi)$ can be monitored by tracking the shift $\Delta V_r = \Delta\Gamma V_{RF}$ in the reflected component of the RF drive signal. This is accomplished by embedding the nanoresonator in a phase-locked loop (Fig. 2). Essentially, a directional coupler routes the reflected signal to a phase-sensitive detector, the output of which is fed into a VCO that supplies $V_{RF}(\omega)$.

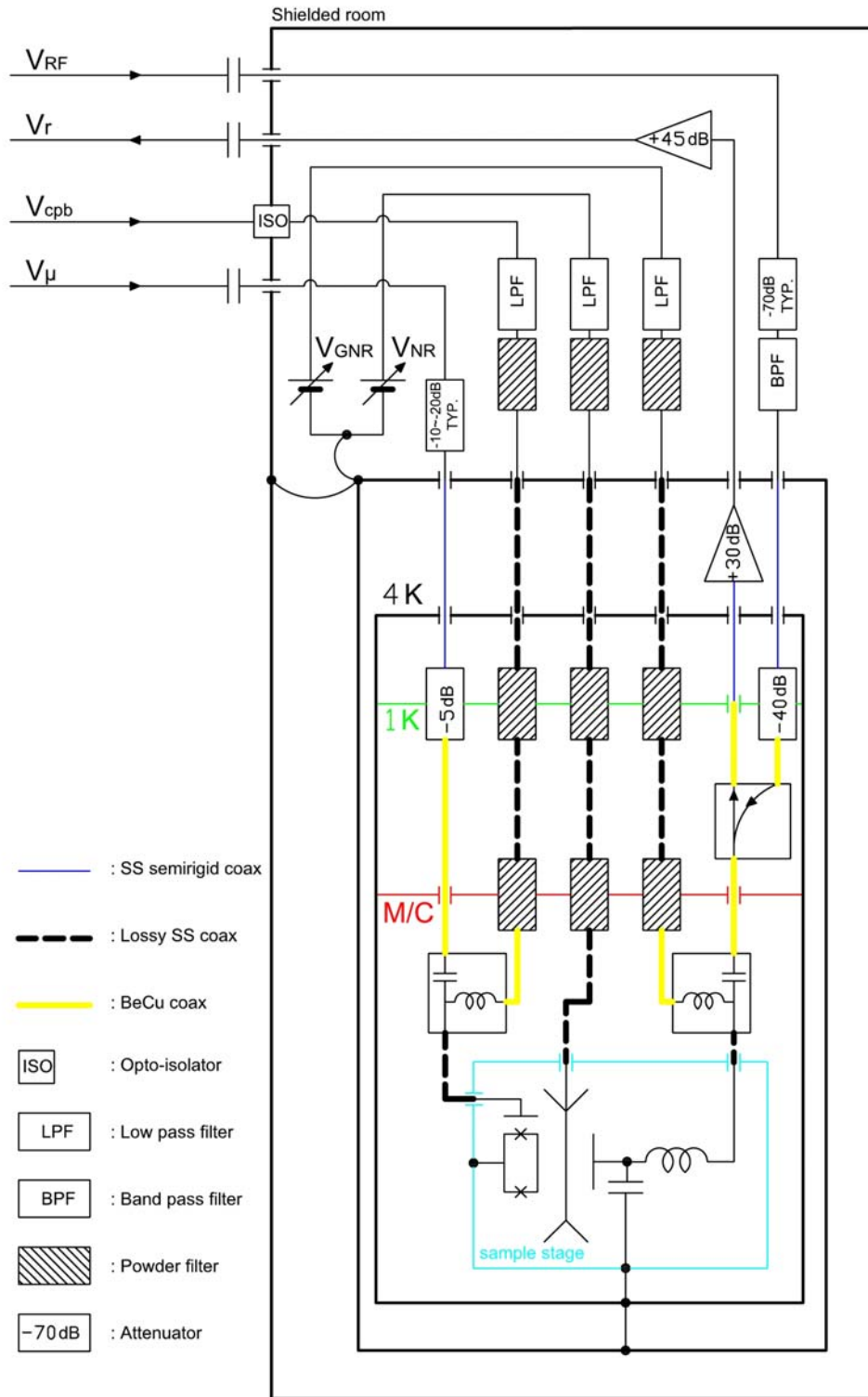


Figure 1: Schematic of measurement circuit

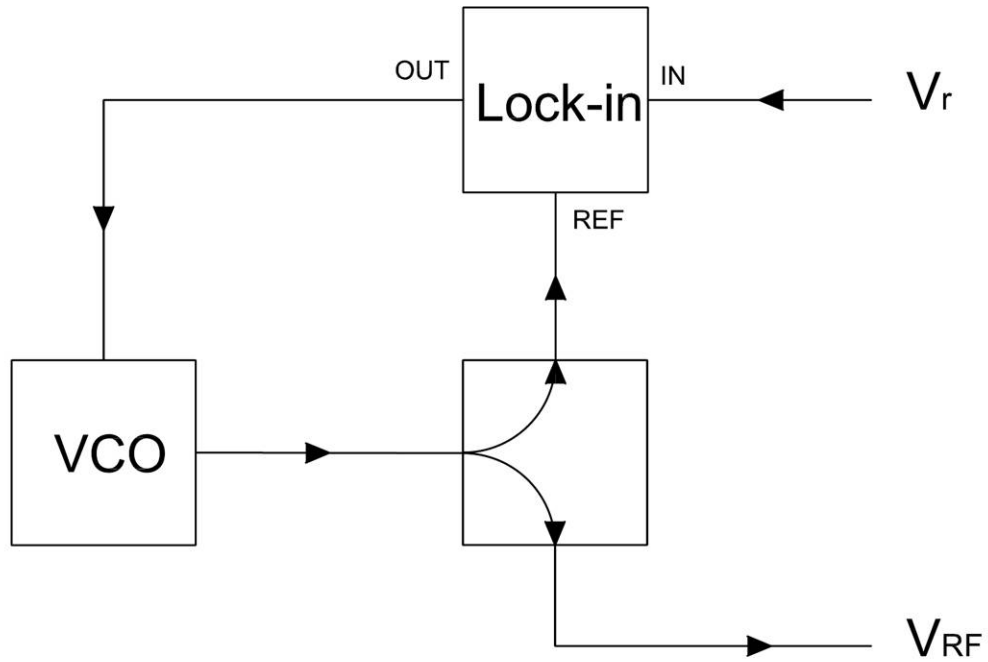


Figure 2: Phase-locked loop circuit

We use a phase-locked loop to measure the nanoresonator frequency shift $\frac{\Delta\omega_{NR}}{2\pi}$. The lock-in acts as a phase detector and the low-pass filter controls the voltage-controlled oscillator (VCO). The VCO output gets split into two signals: one for exciting the nanoresonator (V_{RF}) and the other provides the reference input of the lock-in (REF).

2.4 Results

2.4.1 Dispersive shift of mechanical resonance

In our experiments, the sample is cooled to a temperature $T_{mc} \approx 120-140$ mK at which the qubit predominantly resides in the ground state (i.e., $k_B T_{mc} \ll \Delta E$) and the rate of

quasiparticle poisoning in the qubit is minimal.⁴⁸ We then measure the nanoresonator frequency response using a combination of capacitive displacement transduction and RF reflectometry⁴⁷, (Fig. 3b). Fig. 3c displays the frequency response of the nanoresonator's amplitude (Main) and phase (Inset) at two values of V_{cpb} for fixed Φ and $V_{NR} = 15$ V (the largest coupling voltage used in the experiment). Consistent with Eq. 3 and the CPB residing in the ground state, when V_{cpb} is adjusted to a charge degeneracy point, the nanoresonator experiences a decrease in frequency, the magnitude of which $\left| \frac{\Delta\omega_{NR}}{2\pi} \right| \approx \frac{\hbar\lambda^2}{\pi E_J} = 1600\text{Hz}$ is comparable to $\frac{\kappa}{2\pi}$. For fixed E_J and E_{el} , in agreement with Eq. 3, $\left| \frac{\Delta\omega_{NR}}{2\pi} \right|$ is found to exhibit a quadratic dependence on V_{NR} (bottom inset, Fig. 3c) over the full range of V_{NR} used in the experiment.

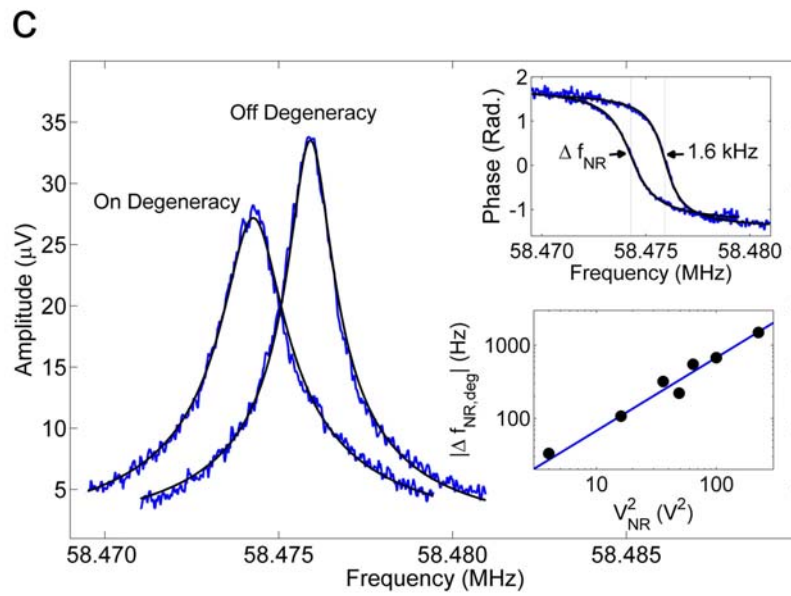
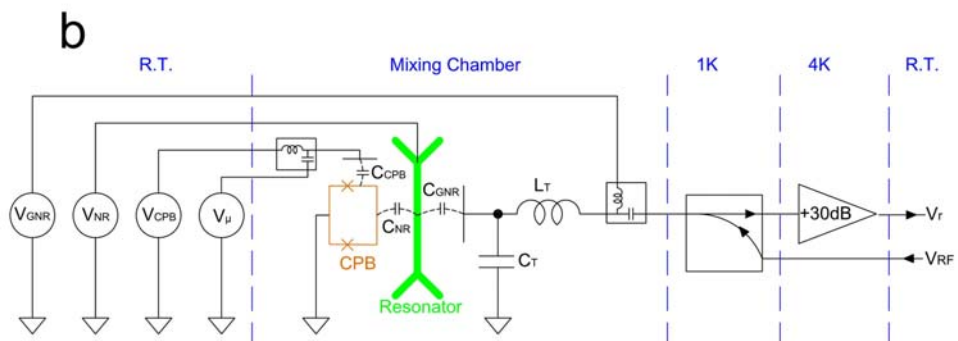
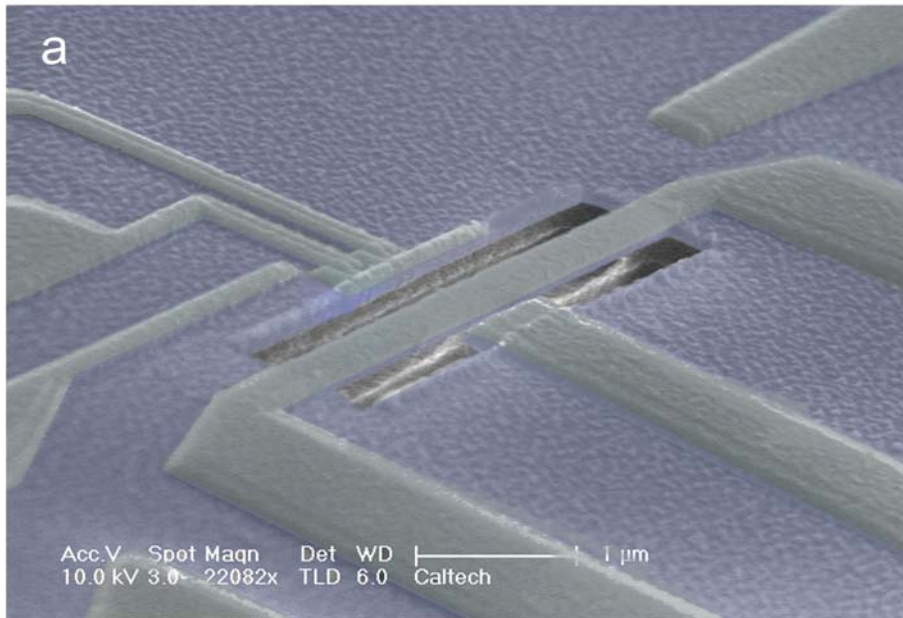


Figure 3: Sample picture, measurement circuit, and measured dispersive shift of mechanical resonance

(a) SEM micrograph of the device. The nanoresonator is formed from SiN with a thin coating (~ 80 nm) of Al for applying the DC voltage V_{NR} . The CPB is formed from Al and located on one side of the nanoresonator at a distance ~ 300 nm. Adjacent to the CPB is an Al electrode for applying V_{CPB} . Another Al gate electrode is situated on the opposite side of the nanoresonator at a distance of ~ 100 nm for actuating the nanoresonator and detecting its response in order to measure $\Delta\omega_{NR}/2\pi$. (b) Measurement circuit for RF reflectometry of the electromechanical impedance. The excitation signal capacitively drives the nanoresonator to an occupation of 10^3 – 10^4 quanta. The tank circuit formed by L_T and C_T serves to transform the electromechanical impedance for matching to a cryogenic amplifier. (c) Frequency response of nanoresonator amplitude (Main) and phase (Inset, Top) for CPB biased on and off of charge degeneracy as measured by RF reflectometry. (Inset, Bottom) Maximum frequency shift of nanoresonator (black circles) for CPB biased on charge degeneracy point as a function of coupling voltage V_{NR} . The solid blue line is a fit to $y = A \cdot V_{NR}^2$, where A is proportionality constant.

2.4.2 Periodicity in V_{cpb} and Φ

Embedding the nanoresonator in a phase-locked loop, we can track $\frac{\Delta\omega_{NR}}{2\pi}$ while keeping V_{NR} fixed and adiabatically sweeping V_{cpb} and Φ (Fig. 4a). We find that the overall dependence of $\frac{\Delta\omega_{NR}}{2\pi}$ on V_{cpb} and Φ is in excellent qualitative agreement with our model (Eq. 3 and Fig. 4b–d). We find that $\frac{\Delta\omega_{NR}}{2\pi}$ exhibits the expected 2e-periodic dependence on V_{cpb} , confirmed for 4 periods. We also observe that the behavior of $\frac{\Delta\omega_{NR}}{2\pi}$ on Φ is in good agreement with the expected periodicity of one flux quantum Φ_0 . At values of Φ for which $E_J/k_B \lesssim T_{mc}$ (e.g., trace 2 in Fig. 4c), the CPB excited state becomes thermally populated in the vicinity of the charge degeneracy points. As a result, the modulation depth of $\frac{\Delta\omega_{NR}}{2\pi}$ is reduced, which can be accounted for by replacing the qubit expectation in Eq. 3 with the Boltzmann-weighted average $\langle \hat{\sigma}_z \rangle = -\tanh\left(\frac{\Delta E}{2k_B T_{mc}}\right)$.

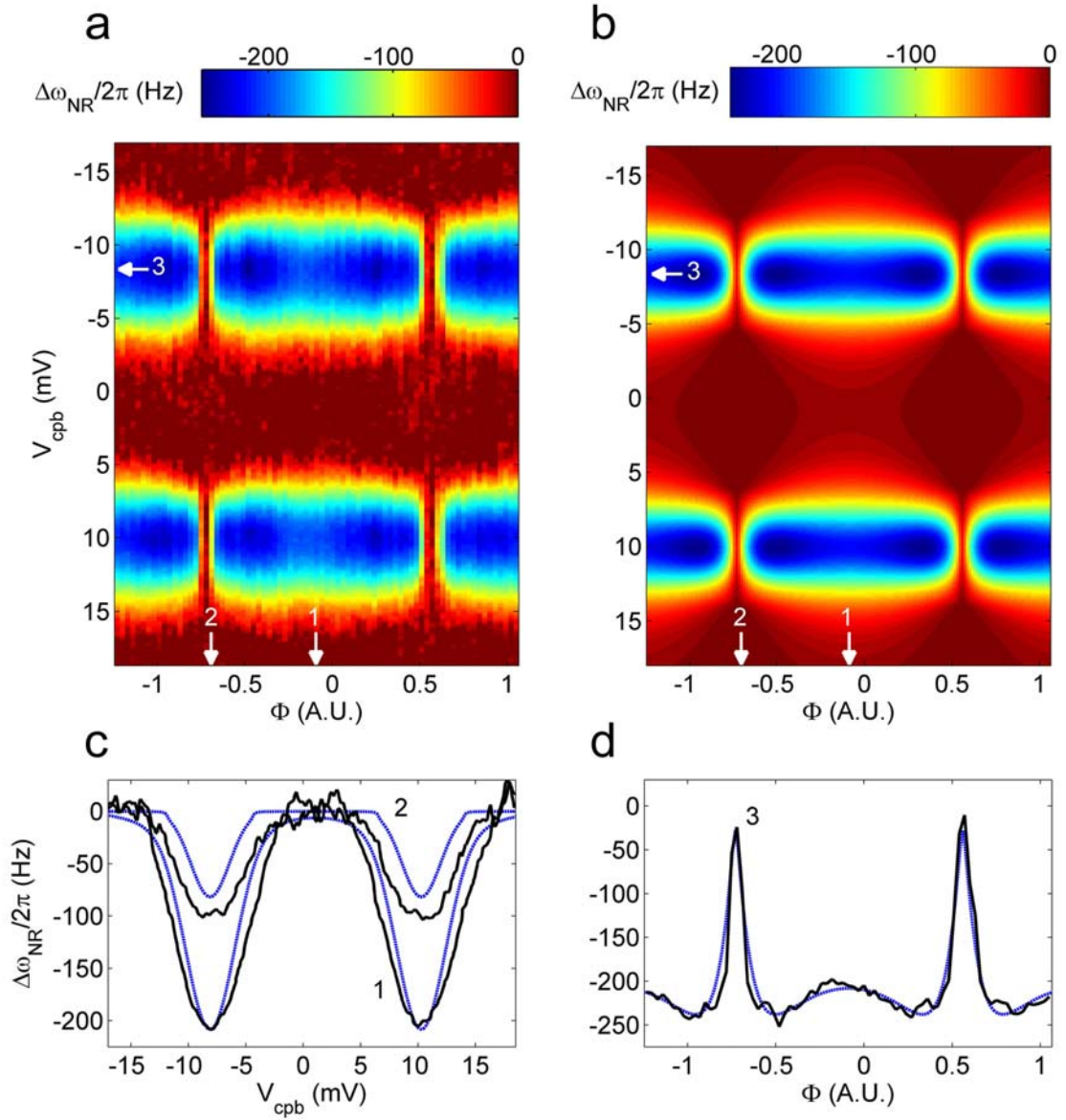


Figure 4: Dispersive shift vs. qubit control parameters

(a) Measured nanoresonator frequency shift $\frac{\Delta\omega_{NR}}{2\pi}$ as a function of CPB gate voltage

V_{CPB} and flux Φ for $V_{NR}=7.0$ V and $T_{mc}\approx 120$ mK. (b) Numerically calculated $\frac{\Delta\omega_{NR}}{2\pi}$ as

a function of V_{CPB} and Φ for $E_c/h= 16.4$ GHz, $E_{J0}/h=13.2$ GHz, and $\lambda/h=1.5$ MHz. The

numerical model uses the full CPB Hamiltonian (Eq. 4) incorporating $n=-5$ to $n=5$ charge

states, to calculate the two lowest CPB eigenstates $|+\rangle$ and $|-\rangle$. The CPB population $\langle \hat{\sigma}_z \rangle$ is then calculated assuming the appropriate Boltzman weighting. To account for low-frequency charge noise, $\langle \hat{\sigma}_z \rangle$ is convolved with a Gaussian of width $\sigma(2e) = 0.09$ in n_{cpb} . (c) Comparison between data and model of selected traces of $\frac{\Delta\omega_{NR}}{2\pi}$ vs. V_{cpb} at constant Φ . (d) Comparison between data and model of $\frac{\Delta\omega_{NR}}{2\pi}$ at a charge degeneracy

Fig. 5a displays the 2e-to-e transition in periodicity of nanoresonator's frequency shift $\Delta\omega_{NR}/(2\pi)$ with respect to V_{cpb} , taken with flux biased so that $E_J \sim E_{J0}$. At a mixing chamber temperature of 120 mK, the periodicity is primarily 2e-periodic with peaks spaced by $\Delta V_{\text{cpb}} = 18.7$ mV, corresponding to a gate capacitance $C_g = 17.1$ aF. At temperatures of 40 mK and below, the quasiparticle poisoning rates greatly exceed the measurement time, and periodicity is primarily e-periodic with peaks spaced by $\Delta V_{\text{cpb}} \sim 9\text{--}10$ mV.

Fig. 5b displays the periodicity in applied flux Φ of $\Delta\omega_{NR}/(2\pi)$ taken at a charge degeneracy point. The average spacing between the peaks is found to be $\Delta B \sim 200$ μT .

While there is large uncertainty in the effective area of the split-junction CPB, we can

estimate the flux periodicity using the geometric area of the CPB loop $A \sim 5 \mu\text{m}^2$. This yields a flux periodicity of $\Delta\Phi \sim 1 \times 10^{-15} \text{ T}\cdot\text{m}^2$ in reasonable agreement with the expected periodicity of one flux quantum $\Phi_0 = 2.07 \times 10^{-15} \text{ T m}^2$. The background increase in ω_{NR} during the course of the measurement was not typical of most magnetic field sweeps, which were taken over a much smaller range.

To convert the x-axis of Fig. 4a–d into units of Tesla it is necessary to add 80 and multiply by 1.3×10^{-4} . The magnetic field sweep was applied on top of a static field of $\sim 0.01 \text{ T}$. For the data taken in Fig. 7, a different current source and larger background field were used. Thus to convert the x-axis of Fig. 7a–d into Tesla it is necessary to multiply by 2.7×10^{-3} .

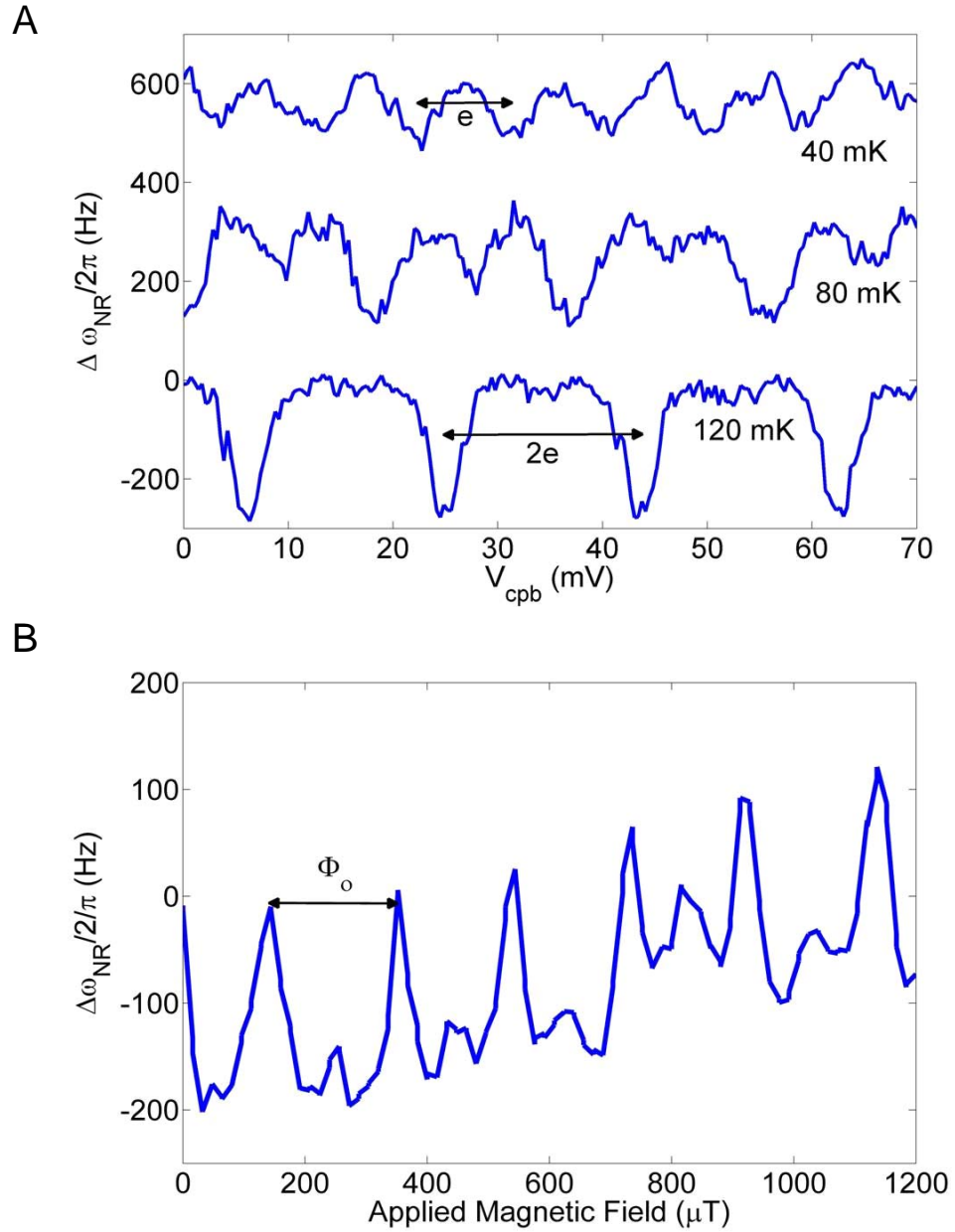


Figure 5: Periodicity in CPB gate charge and flux

(A) $2e$ - e transition of the response in V_{cpb} . Data in (A) taken with $V_{\text{NR}} = 7\text{V}$ and flux bias set so that $E_J \sim E_{J0}$. (B) CPB flux periodicity. Data in (B) taken near a CPB charge degeneracy with $V_{\text{NR}} = 7\text{V}$ and $T_{\text{mc}} \sim 120\text{ mK}$

2.4.3 Correction for charge drift

For a typical “map” measurement, $\Delta\omega_{NR}/(2\pi)$ vs. V_{cpb} vs. Φ , the flux Φ was held constant while we swept V_{cpb} and recorded $\Delta\omega_{NR}/(2\pi)$. The flux was then incremented, and the process repeated. For each constant flux trace, we typically averaged for a couple of seconds. Since the effective gate charge had a slow drift component, a post-processing correction method was employed in order to subtract the drift and to average multiple maps taken over long periods of time. Fig. 6a is the uncorrected $\Delta\omega_{NR}/(2\pi)$ vs. V_{cpb} vs. Φ map for Fig. 4a. In this instance, we chose two charge periods in the map and fit $\Delta\omega_{NR}/(2\pi)$ vs. V_{cpb} to two Gaussian peaks for each value of flux Φ . A typical trace and fit, taken at $\Phi = -0.45$ (A.U.), is displayed in Fig. 6b. The fit gives the positions of the charge degeneracy points and aligns traces taken at successive values of Φ as well as subtracts the offsets due to background fluctuations in $\Delta\omega_{NR}/(2\pi)$, typically on the order of 10 Hz. Fig. 4a is the result of only one post-processed map. For the spectroscopy maps in Fig. 7a–d and the Landau-Zener map in Fig. 11a, as many as 14 maps were taken over the course of a day. The presence of the microwave resonances in these maps made it difficult to fit and find the location of the charge degeneracy points. Accordingly, it was essential, for each value of Φ , to take one trace with microwaves

applied and then a second trace immediately afterward without microwaves applied.

This allowed us to use the maps without microwaves applied to correct the charge drift of the maps with microwaves applied. For better precision, a second post-processing step was used that minimized the variance at each value of Φ between traces of different maps.

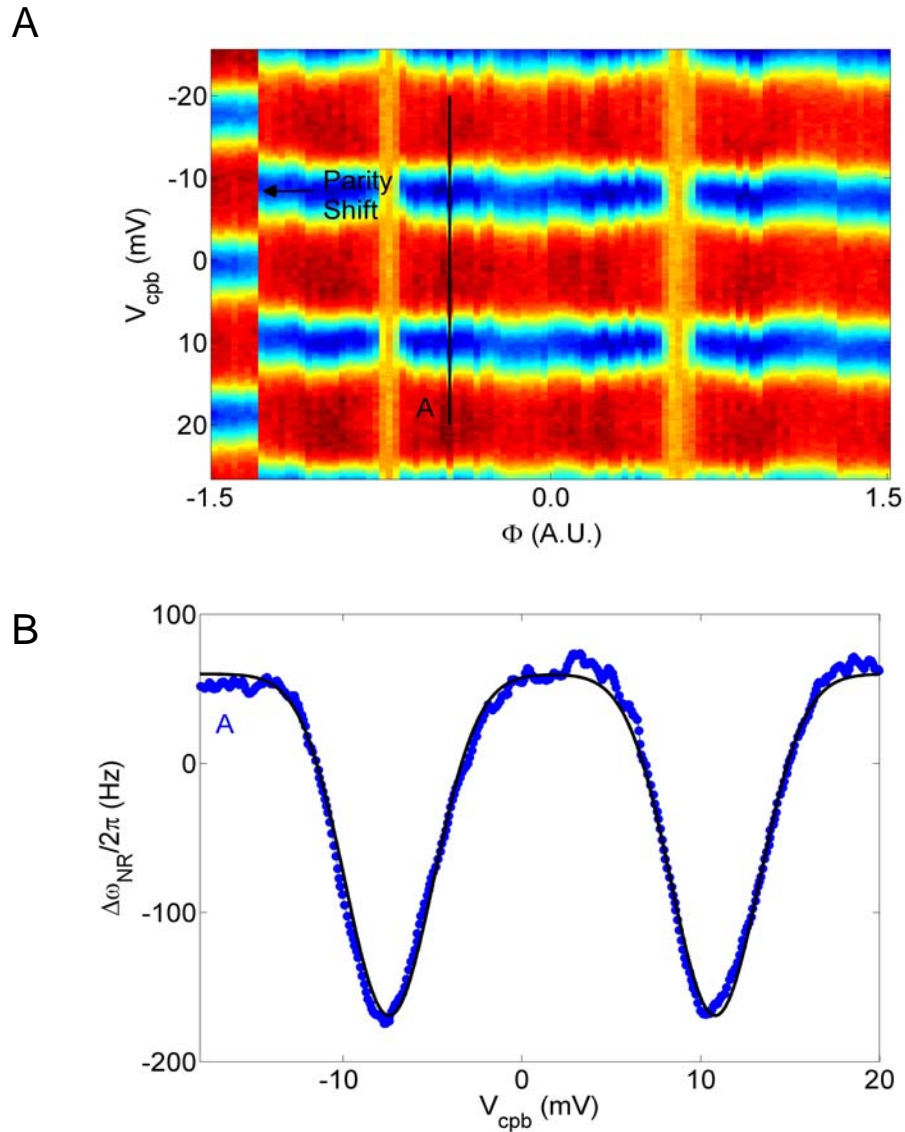


Figure 6: Correction for CPB charge drift

(A) Uncorrected data for Fig. 4. A quasiparticle switching event is evident at $\Phi = -1.3$.

(B) Constant flux cross-section taken at “A”, denoted by vertical black line in (A).

Black line in (B) is a fit of the cross-section “A” to two Gaussian peaks to determine charge-offset and background change from trace-to-trace.

2.4.4 Microwave spectroscopy of CPB

While the CPB state $\langle \hat{\sigma}_z \rangle$ is manipulated by irradiating the CPB gate with microwaves that are resonant with the qubit transition, spectroscopy is carried out by monitoring the mechanical frequency shift $\frac{\Delta\omega_{NR}}{2\pi}$. With the microwave frequency $\frac{\omega_\mu}{2\pi}$ held fixed and the microwave amplitude V_μ adjusted so that $n_\mu = \frac{C_{cpb}V_\mu}{2e} \ll 1$, the CPB oscillates between $|+\rangle$ and $|-\rangle$ with Rabi frequency $\Omega_d \approx \frac{4E_C n_\mu}{\hbar} \frac{E_J}{\Delta E}$ when V_g and Φ are tuned so that $\frac{\Delta E}{2\pi\hbar} \approx \frac{\omega_\mu}{2\pi}$. Because the nanoresonator response time, $\frac{2\pi}{\kappa}$, is long in comparison to the characteristic time scale of the CPB dynamics, measurements of $\frac{\Delta\omega_{NR}}{2\pi}$ reflect the average qubit occupation $\langle \sigma_z \rangle = \rho_+ - \rho_-$, where ρ_+ and ρ_- are found from the steady-state solution to the Bloch equations⁴¹

$$\rho_+ = 1 - \rho_- = \frac{1}{2} \frac{\Omega_d^2 T_1 T_2}{1 + \Omega_d^2 T_1 T_2 + \left(\frac{\Delta E}{\hbar} - \omega_\mu\right)^2 T_2^2} \quad (\text{Eq. 5}).$$

Here T_1 and T_2 are the qubit relaxation and dephasing times, respectively. For n_μ large enough that $\Omega_d^2 T_1 T_2 \gg 1$, the CPB becomes saturated, i.e., $\rho_+ = \rho_- = 1/2$, and $\frac{\Delta\omega_{NR}}{2\pi} \rightarrow 0$. For $\frac{\omega_\mu}{2\pi} = 10.5 - 20 \text{ GHz}$, hyperbola where $\frac{\Delta\omega_{NR}}{2\pi} \rightarrow 0$ appear, tracing out constant energy contours that are in general agreement with the expected (n_{cpb}, Φ) -dependence of the qubit transition ΔE (Fig. 7e).

We can estimate the charging energy E_c and Josephson energy E_J of the qubit from spectroscopy by plotting $\omega_\mu/(2\pi)$ vs. the displacement from degeneracy Δn_{cpb} at which resonance occurs (i.e., $\Delta E = \hbar\omega_\mu$) for fixed E_J . Fig. 8 displays $\omega_\mu/(2\pi)$ vs. Δn_{cpb} for several values of Φ . From the fits to $\omega_\mu/(2\pi) = \sqrt{(8E_c\Delta n_{cpb})^2 + E_J^2}/h$, we find $E_c/h = 13.7 \pm .4$ GHz, $E_c/h = 12.7 \pm .8$ GHz, and $E_c/h = 13.4 \pm .2$ GHz for $\Phi = 0.1\Phi_0$, $0.2\Phi_0$ and $0.35\Phi_0$ respectively. From the intercepts of the fits, we find $E_J/h = 10.4 \pm .5$ GHz, $E_J/h = 9.5 \pm .9$ GHz, and $E_J/h \approx 0$ GHz (large uncertainty) for $\Phi = 0.1\Phi_0$, $0.2\Phi_0$, and $0.35\Phi_0$ respectively. The values of maximum Josephson energy E_{J0} inferred from the fits and the Josephson relation are ~ 10 – 15% smaller than what one would expect from the microwave frequency at which resonance occurs for V_{cpb} and Φ biased such that $\Delta E = E_{J0}$ (Fig. 9a–b, $n_{cpb} = 0.5$ and $\Phi = 0$). Comparing Fig. 9a and Fig. 9b, it is apparent that this occurs for microwave frequencies in the range of $\omega_\mu/(2\pi) = 12.5$ – 13.5 GHz. From these results, our best estimate is $E_{J0}/h \sim 13$ GHz.

Fig. 9 also serves to demonstrate the additional resonance features that appear near charge degeneracy. The dashed green lines denote the resonance bands we expect for the applied microwave frequency $\omega_\mu/(2\pi)$, based upon a calculation of ΔE from the full

Hamiltonian Eq. 4. At the lowest microwave frequencies (Fig. 9a–b), the observed (n_{CPB}, Φ) -dependence of the microwave resonance appears to be consistent with the coupling of the CPB island to an incoherent charge fluctuator.⁴⁹ However, we observed no apparent dependence of the additional resonant features on thermal cycling or the application of background electric and magnetic fields. Additionally, we find that upon increasing $\omega_{\mu}/(2\pi)$ (Fig 9c–d), the qualitative agreement between the observed and expected (n_{CPB}, Φ) -dependence improves.

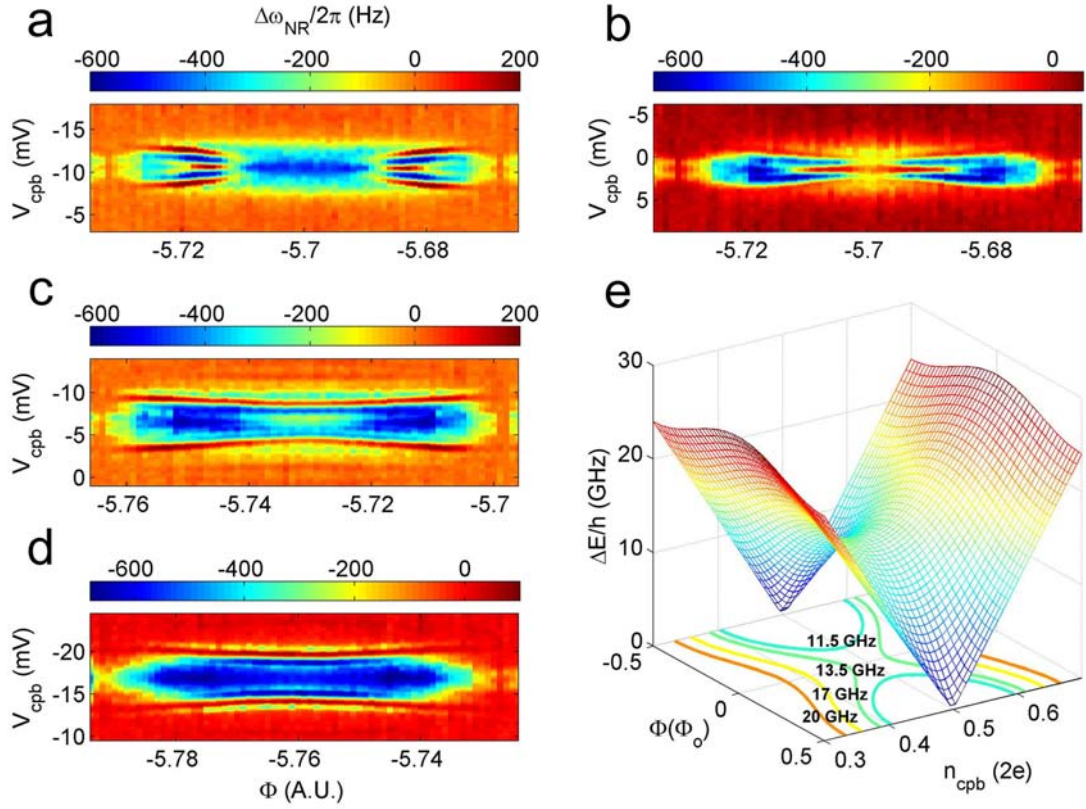


Figure 7: Dispersive shift from weakly driven qubit

Nanoresonator frequency shift $\frac{\Delta\omega_{NR}}{2\pi}$ as a function of V_{cpb} and Φ when microwaves resonant with the CPB ground-excited state splitting are applied. (a) 11.5 GHz, (b) 13.5 GHz, (c) 17 GHz, (d) 20 GHz. (e) Surface plot of CPB ground-excited state splitting ΔE as a function of V_{cpb} and Φ , with constant energy contours at the microwave frequencies highlighted. Data taken with $V_{NR} = 10$ V and $T_{mc} \approx 130$ mK.

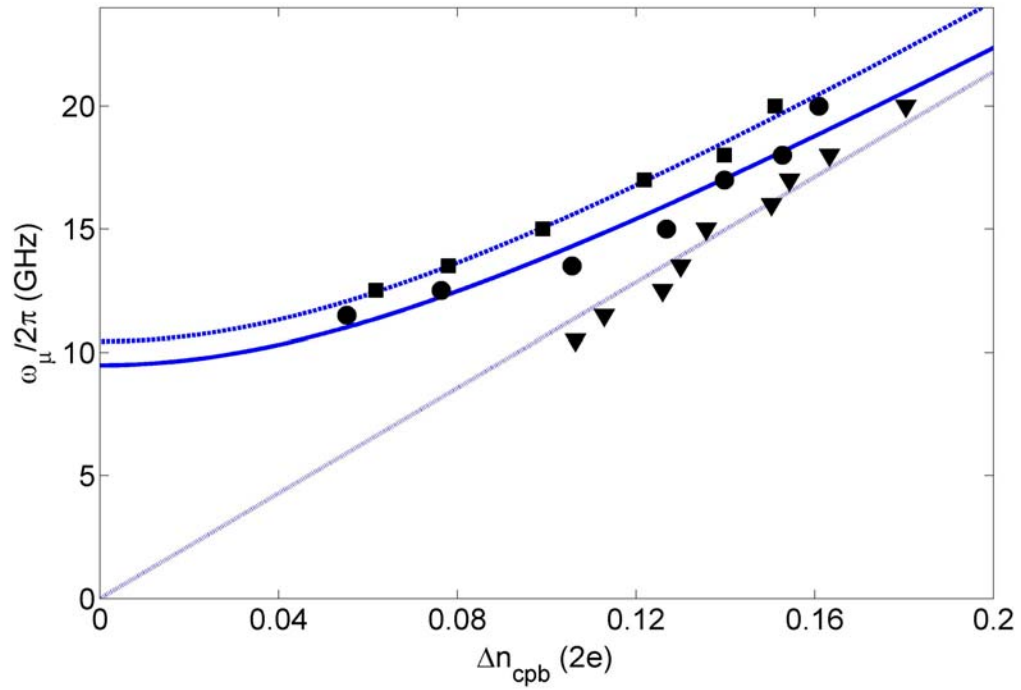


Figure 8: Qubit microwave resonance vs. gate charge

Plot of spectroscopic frequency $\omega_{\mu}/2\pi$ vs. the value of Δn_{cpb} at which the CPB transition energy $\Delta E = \hbar\omega_{\mu}$, for $\Phi=0.1\Phi_0$ (squares), $\Phi=0.2\Phi_0$ (circles), $\Phi=0.35\Phi_0$ (triangles). Data is taken with $V_{\text{NR}} = 10$ V, $T_{\text{mc}} \sim 140$ mK.

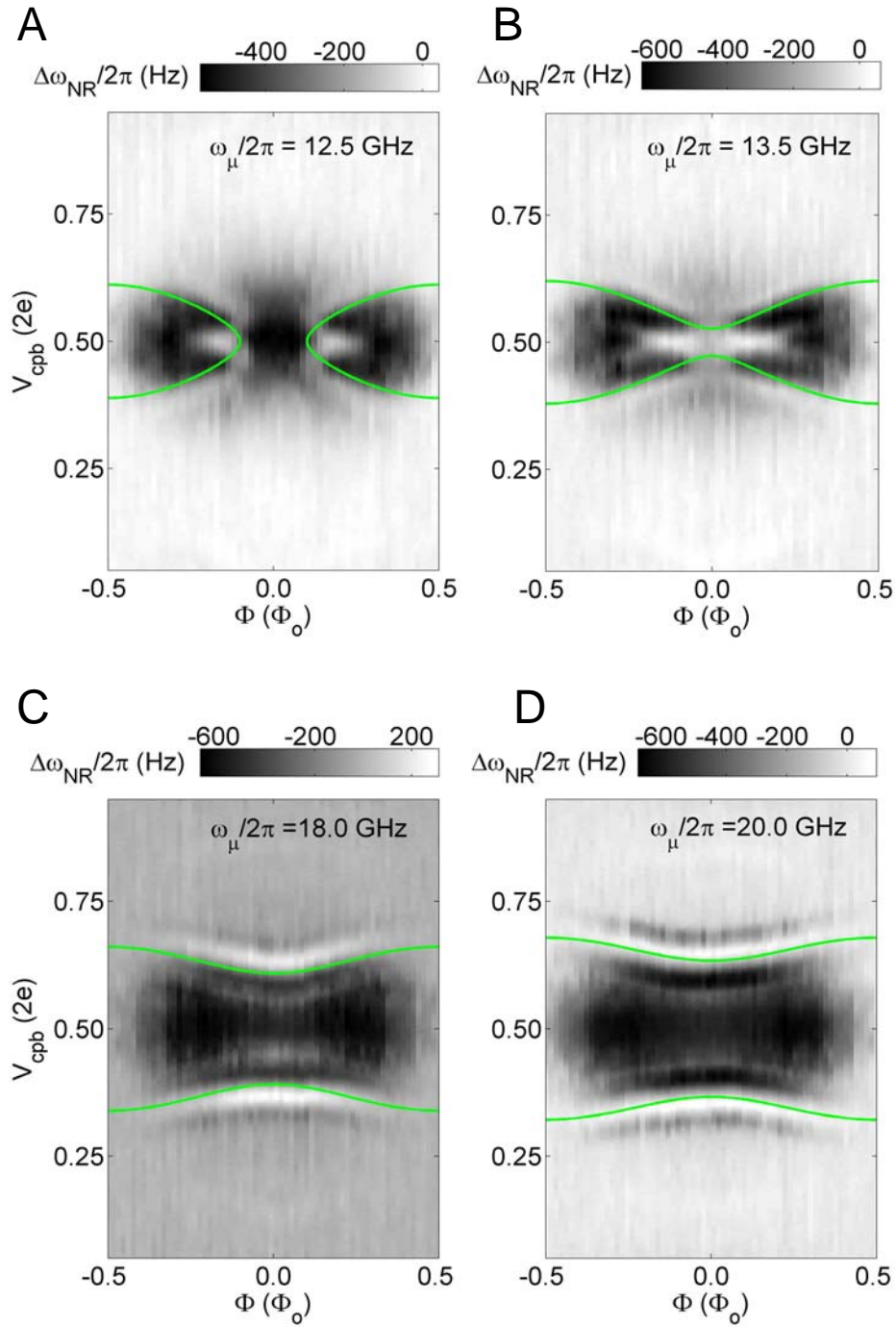


Figure 9: Qubit microwave resonance for different microwave frequencies

Measurements of the nanomechanical frequency shift $\Delta\omega_{NR}/(2\pi)$ vs. V_{cpb} and Φ for

microwave frequencies $\omega_\mu/2\pi = 12.5$ GHz (A), 13.5 GHz (B), 18 GHz (C), and 20 GHz (D). Data taken at $V_{NR} = 10$ V and $T_{mc} = 140$ mK. The experimental values of V_{cpb} and Φ have been converted into units of Cooper pairs and the flux quantum Φ_0 , respectively. The maximum Josephson E_{J0} energy occurs at $\Phi = 0$. When $\hbar\omega_\mu = E_{J0}$, the resonant hyperbola overlap at $\Phi = 0$. Thus, from (A) and (B) we estimate that $E_{J0}/h \sim 13$ GHz. The green lines in the plots denote the expected resonance hyperbola determined from the qubit transition energy ΔE , which we calculate from the full CPB Hamiltonian Eq. 4 using $E_c/h = 14.0$ GHz and $E_{J0}/h = 13.2$ GHz.

Recording the mechanical frequency shift $\frac{\Delta\omega_{NR}}{2\pi}$ as a function of the microwave frequency $\frac{\omega_\mu}{2\pi}$ (Fig. 10) we can extract the driven qubit linewidth

$$\frac{\gamma}{2\pi} = \frac{1}{\pi} \sqrt{\frac{1}{T_2^2} + \frac{\Omega_d^2 T_1}{T_2}} \quad (\text{Eq. 6}).$$

As expected from Ω_d and Eq. 6, we find that $\frac{\gamma}{2\pi}$ increases with increasing V_μ (Inset Fig. 10). From a fit of $\frac{\gamma}{2\pi}$ vs. V_μ^2 to Eq. 6, we find $T_2 \geq 2$ nsec at charge degeneracy.

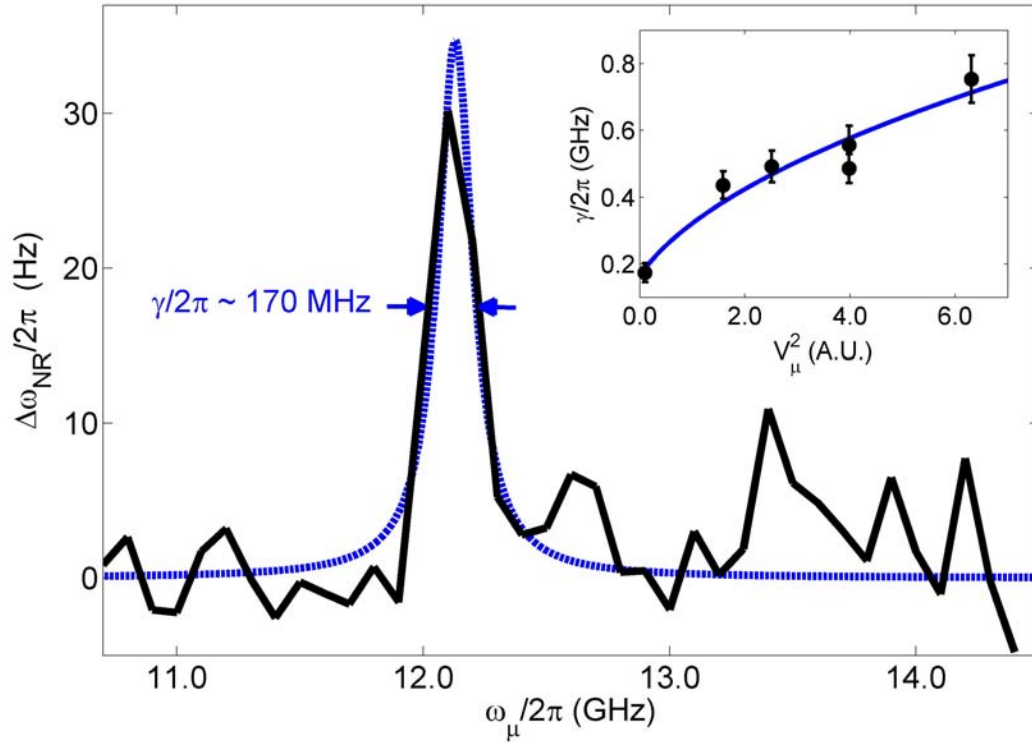


Figure 10: Estimate of qubit linewidth

(Main) Nanoresonator frequency shift $\frac{\Delta\omega_{NR}}{2\pi}$ as a function of $\frac{\omega_{\mu}}{2\pi}$ at the smallest value of microwave amplitude V_{μ} used in the experiment. The solid blue line is a fit to a Lorentzian. (Inset) The linewidth of the transition between CPB states $|+\rangle$ and $|-\rangle$ plotted as a function of V_{μ}^2 . Error bars are from a fit of each $\omega_{\mu}/(2\pi)$ -sweep to a Lorentzian, and they denote the 68% confidence level. The solid-line is a fit to Eq. 6, demonstrating expected broadening of CPB transition due to increased microwave drive. Data is taken with flux biased such that $E_J/h \approx 12$ GHz.

2.4.5 Landau-Zener tunneling of CPB with strong microwave excitation

At large microwave amplitude V_μ ($n_\mu \gtrsim \frac{E_J^2}{\hbar\omega_\mu E_C}$), we demonstrate that we can utilize the nanomechanical frequency shift $\frac{\Delta\omega_{NR}}{2\pi}$ as a probe of quantum coherent interference effects in the CPB (Fig. 11). These effects arise as a result of Landau-Zener (LZ) tunneling⁵⁰ that can occur between $|-\rangle$ and $|+\rangle$ whenever the CPB is swept through the avoided-level crossing at charge degeneracy. If T_2 is longer than the microwave modulation period $\frac{2\pi}{\omega_\mu}$, then successive LZ events can interfere, resulting in oscillations in the qubit population $\langle \hat{\sigma}_z \rangle$ as a function of V_μ and V_{cpb} .

By monitoring $\frac{\Delta\omega_{NR}}{2\pi}$ while sweeping V_{cpb} at fixed values of V_μ , we clearly observe quantum interference (Fig. 11a). At the lowest-values of V_μ , LZ tunneling is exponentially suppressed,⁵⁰ and we observe a dependence of $\frac{\Delta\omega_{NR}}{2\pi}$ on V_{cpb} consistent with the CPB residing in $|-\rangle$. As V_μ is increased, we observe that $\frac{\Delta\omega_{NR}}{2\pi}$ oscillates with V_μ and V_{cpb} , and even changes sign. It becomes maximally positive at values of V_μ and V_{cpb} where we expect the occupation of $|+\rangle$ to be maximum (the intersections of the contours in Fig. 11a). We observe that the spacing ΔV_{cpb} in the gate voltage between

adjacent interference fringes increases linearly with increasing microwave frequency $\frac{\omega_\mu}{2\pi}$ (Fig. 11b–c) as expected. A fit of Δn_{cpb} vs. $\frac{\omega_\mu}{2\pi}$ (Fig. 11c) yields $E_c = 15 \pm 1$ GHz, which is in good agreement with the value extracted from spectroscopy. Figure 11d displays a cross-section of $\frac{\Delta\omega_{NR}}{2\pi}$ vs. V_μ taken at charge degeneracy, demonstrating the expected periodic dependence and Lorentzian shape of the interference maxima. The primary maxima in $\frac{\Delta\omega_{NR}}{2\pi}$ occur at values of V_μ that produce a phase shift of $2\pi m$, where m is an integer, in the CPB's wave function over one-half cycle of the microwave modulation. The resulting periodicity in V_μ provides an estimate of ~ -44 – 48 dB of the total attenuation at $\frac{\omega_\mu}{2\pi} = 6.50$ GHz in the CPB gate line, which is in reasonable agreement with measurements of the attenuation at room temperature.

The contour lines overlaying the Landau-Zener interferogram in Fig. 11a denote locations in (V_{cpb}, V_μ) -space where the phase of the CPB wavefunction is a multiple of 2π . These contours were generated via the same method used in Sillanpää et.al.⁵⁰, with $\varphi_{L,R} = \frac{1}{\hbar} \int_{t_0}^{t_2} dt \Delta E(n_{cpb}(t)) - 2\varphi_S$. For a given V_{cpb} and V_μ , “L” and “R” correspond to the phase φ_L developed while the CPB traverses points to the left of charge degeneracy (i.e., $V_\mu < -3.66$ mV) and the phase φ_R developed while the CPB traverses points to

the right of charge degeneracy (i.e., $V_\mu > -3.66\text{mV}$) respectively. The Stokes phase φ_s , is also as defined in Sillanpää et.al.⁵⁰. The parameters used to generate the overlay were $E_c/h = 14.0\text{GHz}$, $E_{J0}/h = 13.2\text{GHz}$, $C_g = 17.1\text{aF}$, and $\omega_\mu/(2\pi) = 6.5\text{GHz}$. Also, a factor of 2.8 was used to convert n_μ into V_μ , corresponding to an attenuation of 43.5 dB. Transmission measurements of the microwave circuit made at room temperature using a network analyzer with a $50\ \Omega$ input impedance yield $\sim 50\text{--}54$ dB attenuation. This is in reasonable agreement with value extracted from the LZ interferogram, considering that the CPB gate presents an effectively open-circuit termination to the microwave line during operation.

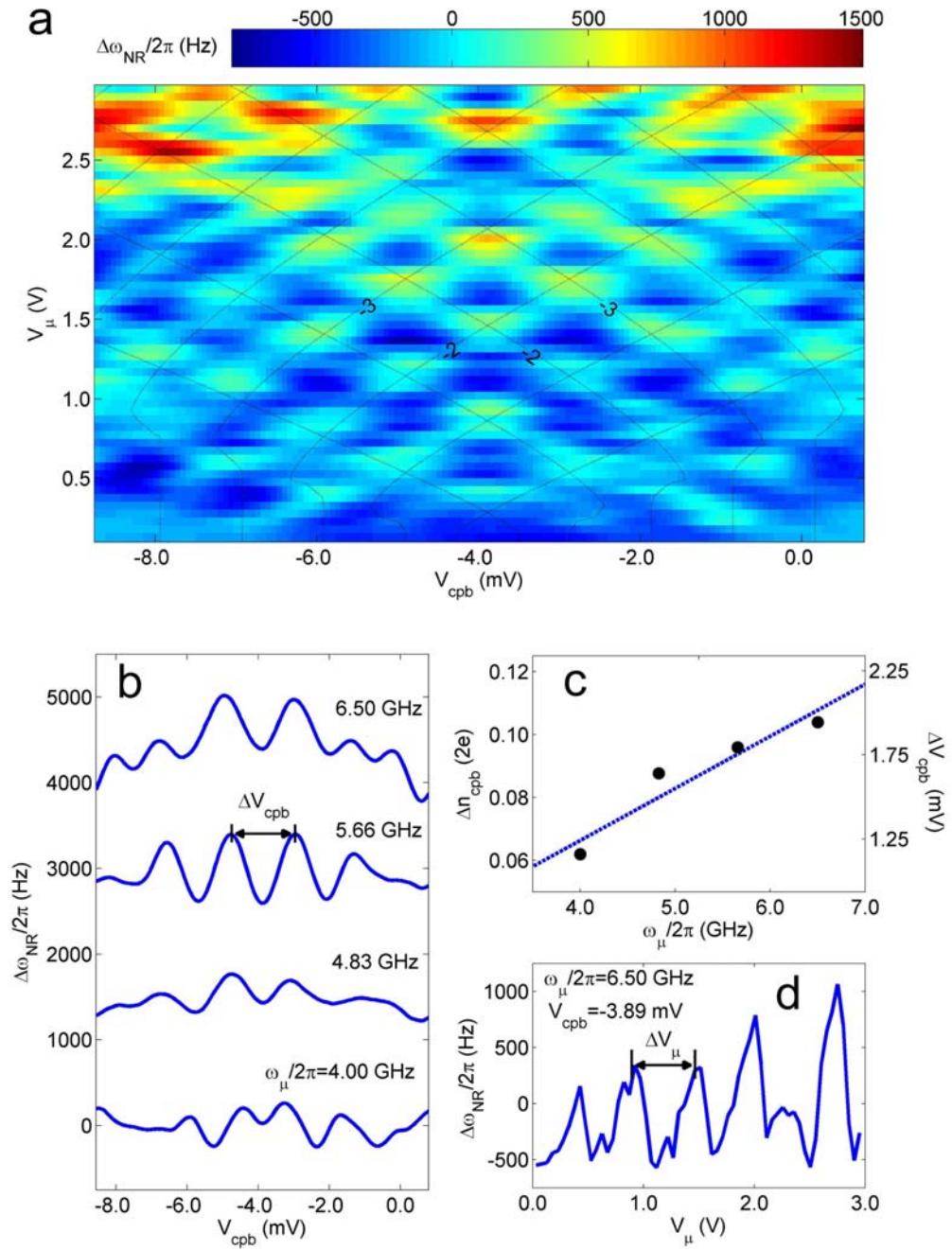


Figure 11: Landau-Zener interference with strong qubit excitation

Landau-Zener interferometry performed using the nanomechanical frequency shift as a

probe. (a) Interference fringes plotted as a function of microwave amplitude n_μ and CPB gate voltage n_{cpb} . (b) For $\frac{\omega_\mu}{2\pi} = 4.0 - 6.5 \text{ GHz}$, cross-sections of constant n_μ , are displayed, chosen to coincide with the intersection of the $m=-2$ and $m=-3$ constant phase contours. (c) Linear fit of the spacing Δn_{cpb} between adjacent interference fringes at intersection of the $m=-2$ and $m=-3$ constant phase contours. Δn_{cpb} is determined from a fit of adjacent peaks ($m=-2,-3$) and ($m=-3,-2$) to a double Gaussian. (d) Nanomechanical frequency shift vs. microwave amplitude for $\frac{\omega_\mu}{2\pi} = 6.5 \text{ GHz}$ at $V_{cpb} = -3.89 \text{ mV}$, demonstrating the expected periodicity in the interference fringes

For both driven and un-driven CPB cases, it is rather remarkable how well the simple dispersive model (Eq. 3) agrees with our observations. It is not obvious, *a priori*, that the same equations of motion used to model the interaction between an atom and a photon should also apply to the interaction between a suspended nanostructure and a mesoscopic electronic device, given the latter systems are each comprised of billions of atoms. Despite this agreement, several outstanding issues are noteworthy. First, we observe increased damping of the NEMS upon tuning the CPB to the charge degeneracy point. While it is necessary to take more data to determine the origin of this excess energy loss, the fact that it depends on the CPB gate bias V_{cpb} and increases with V_{NR}

suggests that it is mediated by the CPB. Second, we observe additional resonant features near charge degeneracy (Figs. 7 and 9) whose origins are not yet understood. These robust features do not appear to be sensitive to time or background electric field. Further, they also do not demonstrate a clear dependence on n_μ , suggesting that mechanisms such as multi-photon transitions⁵¹ or Landau-Zener tunneling⁵⁰ may be ruled out.

2.5 Discussion

The coupling strength, λ , which is achieved in this experiment is sufficiently large to realize many recent proposals for quantum nanomechanical measurements^{23, 27, 31-38}.

With our currently-realized value of λ , it should already be possible to generate nanomechanical “laser” states by tuning the Rabi frequency of the driven qubit into resonance with the nanoresonator (i.e., $\Omega_d \approx \omega_{NR}$), and stimulating a coherent exchange of energy between the nanoresonator and the dressed states of the qubit.³⁵ This resonance condition should now be achievable, since we estimate that at charge degeneracy, for the range of V_μ explored in the spectroscopy reported here, $\frac{\Omega_d}{2\pi} \sim 10 - 250$ MHz .

Furthermore, with only either a threefold increase in the nanomechanical frequency, $\frac{\omega_{NR}}{2\pi}$, or a threefold reduction in qubit linewidth, $\frac{\gamma}{2\pi}$, the proposal for side-band-resolved cooling of the nanoresonator close to its quantum ground state could be pursued.²⁷

The qubit-NEMS coupling strength, λ , can be increased by a factor of 10 or more by engineering a smaller electrode gap, $d = 85$ nm, and maintaining $V_{NR} = 15$ V. These parameters have already been demonstrated with single-electron transistors.¹⁵ Such significant, yet realistic improvement to the coupling, along with the implementation of circuit-QED (cQED) architecture⁵² to reduce qubit damping and provide independent read-out of the qubit, should push these experiments into the strong-dispersive limit,

$\frac{2\lambda^2}{(\Delta E - \hbar\omega_{NR})} > \hbar\gamma$, thereby enabling a variety of advanced quantum measurements. One

possibility is utilizing the complimentary CPB “Stark shift”

$\frac{\Delta E_{Stark}}{2\pi\hbar} = \frac{\hbar\lambda^2}{\pi} \frac{E_J^2}{\Delta E(\Delta E^2 - (\hbar\omega_{NR})^2)} (2 \langle \hat{N} \rangle + 1)$, which arises from the dispersive

interaction, to perform QND measurements of nanomechanical Fock states²³. Thus, rather

than monitoring $\frac{\Delta\omega_{NR}}{2\pi}$ to observe the state of the qubit, as done in these experiments,

one would monitor $\frac{\Delta E_{Stark}}{2\pi\hbar}$, either via Ramsey interferometry or direct spectroscopy to

infer the number state of the nanoresonator.

These realistic prospects for performing a wide array of quantum measurements establish the qubit-NEMS resonator system as a new tool with which to explore the quantum mechanics in macroscopic systems.

Chapter 3

Parametric amplification and back-action noise squeezing by driven Cooper-pair box qubit

Parametric amplifiers have been essential in manipulating the quantum noise of optical⁵³⁻⁵⁷ and microwave electromagnetic fields⁵⁸⁻⁶⁰. At the heart of such experiments, reactive media, including optical crystals, atomic clouds, and Josephson junctions, are strongly driven so that nonlinearities in the media stimulate processes that can be used for signal amplification and vacuum noise squeezing.

Similarly, nonlinearities in micro- and nano-electromechanical systems (MEMS and NEMS) have been utilized for parametric amplification of motional signals before transduction to the electronic domain⁶¹⁻⁶⁴, and demonstrating thermal noise squeezing⁶⁴.

While several different techniques have been explored for parametric modulation of NEMS and MEMS, the most common approach utilizes the shift in mechanical resonance frequency that results from the electrostatic nonlinearity of a nearby electrode^{3, 64}.

In principle, parametric modulation via this capacitive “pulling” should enable the preparation of quantum squeezed states of motion⁶⁵. However, due to the microscopic scale of such systems, geometric capacitances are typically very small. Thus, to achieve enough parametric gain to reach the quantum limit or generate quantum squeezed states, large pump amplitudes are required, and those could result in deleterious effects that obscure quantum signatures. For example, assuming the parameters realized in a recent experiment⁶⁶, squeezing the mechanical noise to 10% of the vacuum level would require modulating the gate electrode of the nanoresonator with an amplitude of 300 mV. Operating with such a large pump amplitude could present technical challenges; for example, parasitic coupling to ultra-sensitive measurement electronics such as a single-electron transistor or charge qubit.

In contrast, the new method shown here utilizes the highly nonlinear charge-voltage relationship in a Cooper-pair box (CPB) qubit that results from the Josephson coupling across the CPB's superconducting tunnel junctions. When the nanoresonator is capacitively coupled to the CPB, this charge-voltage relationship affects the nanoresonator's motion and its resonance shows a CPB-state-dependent shift¹³. We find

the modulation of the qubit gate voltage produces parametric response of the nanoresonator that is 3000 times greater than what can be achieved using the geometric capacitance alone. The use of the qubit nonlinearity to parametrically pump the nanoresonator also significantly reduces the direct electrostatic drive of the resonator, which occurs simultaneously with parametric modulation when pumping through geometric capacitance⁶⁷. This further complicates protocols for engineering non-classical states of the mechanics. Also, phase-sensitive detection can be utilized for position measurements with sensitivity below the quantum limit for continuous phase-insensitive detection^{68, 69}. Furthermore, recent theoretical studies^{70, 71} have shown that a driven CPB can be used as an auxiliary system with which to generate various nonlinear nanomechanical Hamiltonians, opening up the possibility for producing a variety of non-classical states of nanoresonators.

3.1 Parametric excitation of harmonic oscillator: amplification and noise squeezing

When the spring constant of a harmonic oscillator is modulated at twice its resonance frequency, i.e., $k_{eff} = k_0 + \delta k \cos(2\omega_0 t)$, the oscillator amplitude is larger than the case

without the parametric modulation (or “pump”). The resulting gain G is given by⁶⁴ (Appendix C),

$$G = \sqrt{\left(\frac{\cos \varphi}{1 + Q\delta\omega/\omega_0}\right)^2 + \left(\frac{\sin \varphi}{1 - Q\delta\omega/\omega_0}\right)^2} \quad (\text{Eq. 7})$$

where ω_0 is the resonant frequency, φ is the phase of the force on the resonator relative to the pump, and a small δk is assumed ($\delta k/k_0 \approx 2\delta\omega/\omega_0$). When $\varphi = \pi/2$ the gain is maximized, and as $\delta\omega \rightarrow \omega_0/Q$ the resonator becomes unstable and self-oscillates. On the other hand, when $\varphi = 0$, the gain is minimized and approaches a value of 1/2 as $\delta\omega \rightarrow \omega_0/Q$. When the nanoresonator is driven by a random noise force, this deamplification results in noise squeezing⁶⁴.

The coupling to the CPB induces a frequency shift in the nanoresonator given by Eq. 3.

This resonance shift $\Delta\omega_{NR}$ is effectively the change in the nanoresonator’s spring constant, k_{eff} . When $\Delta\omega_{NR}$ is modulated via qubit excitation at twice of ω_{NR} , such

$$\text{that } \Delta\omega_{NR} = \Delta\omega_{NR,0} + \frac{\partial(\Delta\omega_{NR})}{\partial n_{cpb}} \delta n_{cpb} \cos(2\omega_{NR}t), \delta k_{eff} = \frac{2k_{eff}}{\Delta\omega_{NR,0}} \frac{\partial(\Delta\omega_{NR})}{\partial n_{cpb}} \delta n_{cpb} \cos(2\omega_{NR}t)$$

gives the parametric excitation.

3.2 Setup and results

Fig. 12a shows the schematic of the measurement circuit. Except for the addition of a parametric drive, the cryogenic and electronic set-up are identical to the experiment described in the previous chapter. Figure 12b is the measured resonance shift $\Delta f = \Delta\omega_{NR} / 2\pi$ when the qubit is in the ground state, plotted as a function of the flux Φ applied to the qubit and the qubit gate voltage $V_G = 2q_e n_g / C_G$ (q_e =electron charge). In the map, we pick the constant flux section (dashed vertical line in Fig. 12b) where the frequency shift at the charge degeneracy is the maximum. The resulting trace of Δf vs. V_G is shown in Fig. 12c and fits well to the expected dependence given by Eq. 3. This fit gives $E_C / h = 12.5$ GHz and $\lambda / h = 3.2$ MHz. These values agree with the spectroscopic measurements in the previous chapter⁷². We fix V_G so that Δf is half of the value at degeneracy (the bias point is denoted by the green cross in Fig. 12(c)). At this bias point, the parametric pump modulation is given approximately by $\delta\omega / 2\pi \approx \partial(\Delta f) / \partial V_G \cdot V_{2\omega}$, where $\partial(\Delta f) / \partial V_G$ is the linear parametric response and $V_{2\omega}$ represents a small modulation of qubit gate bias. From the measured dependence of Δf on V_G , we deduce $\partial(\Delta f) / \partial V_G = 1.1$ kHz/mV by comparing with a numerical calculation. To compare this with the geometric capacitance effect of the qubit gate, we sweep V_G and separately measure the resonance shift without coupling to the qubit ($V_N = 0$ V). From this we obtain

$\partial(\Delta f)/\partial V_G = 0.3$ Hz/mV, which is approximately a factor of 3000 smaller than the parametric response using the CPB.

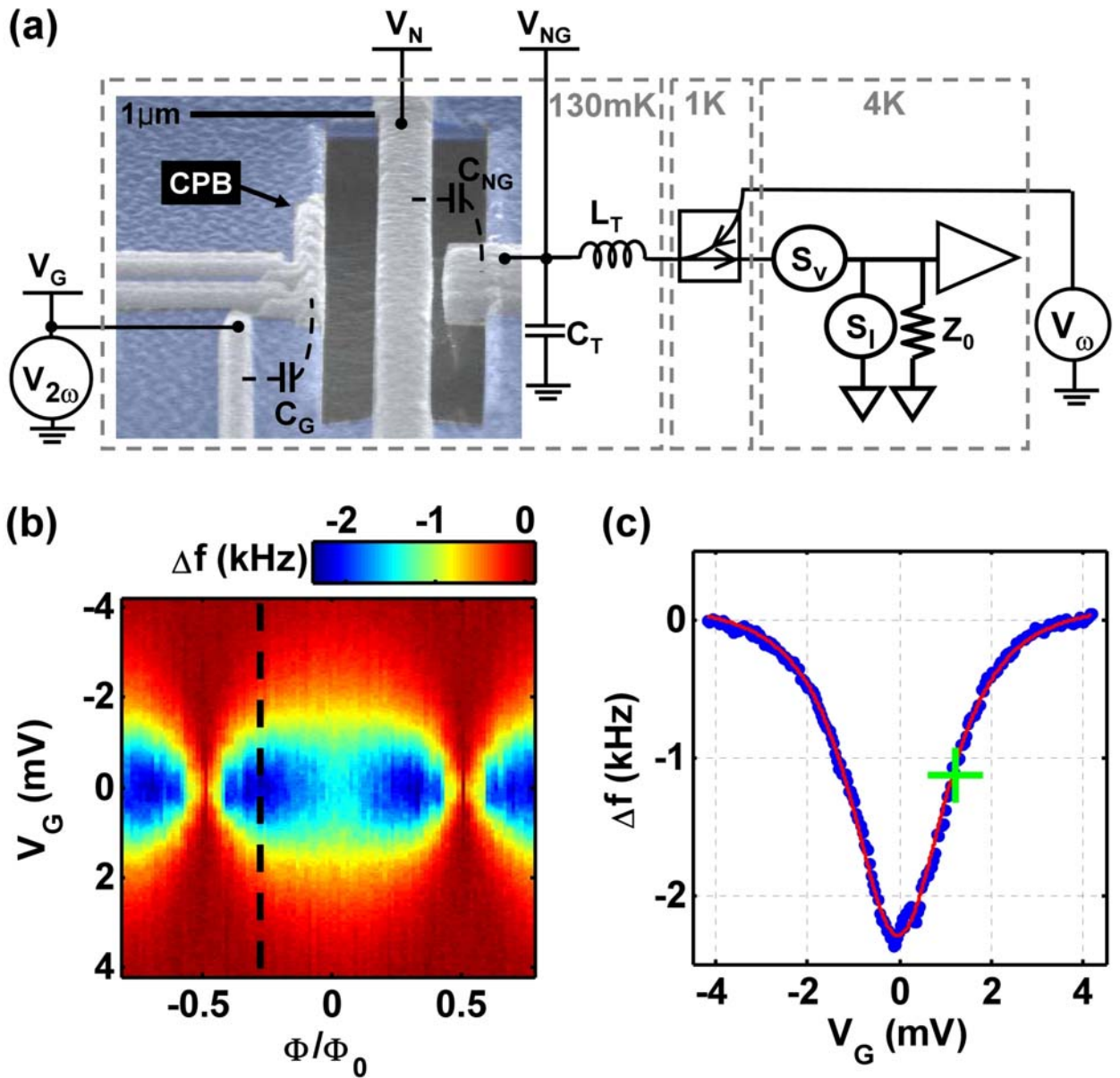


Figure 12: Scanning electron micrograph of the device and the measurement circuit diagram

The sample picture is colored to show different materials — silicon nitride (blue) and aluminum (gray). The matched cryogenic amplifier ($Z_0 = 50\Omega$) is modeled to have two uncorrelated sources of noise, S_V for the voltage noise density and S_I for the current

noise density. (b) Color map of resonance frequency shift ($\Delta f = \Delta\omega_{NR}/(2\pi)$) vs. CPB gate voltage (V_G) and flux (Φ) where Φ_0 is flux quantum. (c) Δf as a function of gate voltage (blue circles), representing the constant-flux cross-section that is indicated in (b) by the vertical dashed line. Red line displays a fit of the data to Eq. 3. The green cross is the bias point at which parametric response measurements are performed.

3.2.1 Parametric amplification and oscillation

To obtain parametric amplification, we set V_G and Φ , then turn on the resonator excitation $V_\omega \cos(\omega_0 t + \varphi)$ and apply the pump $V_{2\omega} \cos(2\omega_0 t)$ to the CPB gate electrode. Fig. 13a shows a typical sweep of nanoresonator amplitude vs. φ under these conditions. A clear periodicity in φ with period π is observed in good agreement with Eq. 7. In Fig. 13b, φ is set at $\pi/2$ and $V_{2\omega}$ is swept for three different values of resonator excitation V_ω . For pump amplitudes up to $V_{2\omega} \cong 0.8$ mV, the data fits well to Eq. 7 and indicates that the threshold for self-oscillation is 1 mV. Well above this threshold, in Fig. 13c, we clearly observe regions in the qubit parameter space, centered about maxima in $|\partial(\Delta f)/\partial V_G|$, where the nanoresonator becomes unstable and self-oscillates.

3.2.2 Nonlinear dissipation

It is evident from Fig. 13b, that the parametric gain saturates above $V_{2\omega} = 1\text{mV}$. Gain saturation occurs at lower values as the resonator excitation V_{ω} is increased, occurring at approximately the same mechanical amplitude for each value of V_{ω} . For a pump amplitude of $V_{2\omega} = 1.2\text{mV}$, we estimate the saturation amplitude to be $x = 9\text{pm}$. This is much smaller than the critical amplitude for the elastic Duffing nonlinearity⁷³, which we estimate to be 1.4 nm. Higher-order terms in the parametric response $\Delta f(V_G)$ are also too small to account for the observed saturation. We believe that it can be explained by a general model⁷³⁻⁷⁵ that incorporates a nonlinear damping force $\eta x^2 \dot{x}$ on the nanoresonator. Such dissipative effects have been observed in similar parametrically-driven mechanical resonators by other groups⁷⁶, and an analogous nonlinear damping is known to exist in superconducting microwave resonators⁷⁷. We use secular perturbation theory⁷³ to account for the additional nonlinear damping and derive the nanoresonator's amplitude X in response to a harmonic force $F \cos(\omega_0 t)$. We find it to satisfy

$$\frac{\delta k - \delta k_c}{\delta k_c} = \frac{\eta Q \omega_0}{4k_{\text{eff}}} X^2 - \frac{Q}{k_{\text{eff}}} \frac{F}{X} \quad (\text{Eq.8})$$

where δk_c is the amplitude of the spring constant modulation at the self-oscillation threshold.

To fit the data, as shown in Fig. 13b, Eq. 8 is first simplified to $y = Ax^2 + B/x + C$ and then used fit with variables x =(mechanical displacement X before normalization) and $y = V_{2\omega}$. With the calculated fit parameters, a cubic equation $AX^3 + (C - V_{2\omega})X + B = 0$ is solved for each $V_{2\omega}$ and this produces the solid curves in Fig. 13b. From the fit, we deduce a nonlinear dissipation coefficient $\eta \cong 8 \times 10^9 \text{ kg/m}^2\text{s}$ for these measurements. This is within an order-of-magnitude of an estimate of $\eta \approx 1 \times 10^9 \text{ kg/m}^2\text{s}$, the value we calculate numerically from the measured dependence of nanoresonator damping vs. qubit gate voltage V_G . The PLL circuit employed in the resonance shift measurement also monitors the magnitude simultaneously, giving us information about the nanoresonator's quality factor with respect to the gate charge. Fig. 14 shows the width of the nanomechanical resonance ($\gamma = \omega_0 / Q$) deduced from the measured quality factor. It is clear that additional dissipation arises due to coupling to the CPB, which this becomes maximal at the degeneracy point. We have not clearly identified the source of this additional dissipation. One possible explanation may be the resonance frequency fluctuations due to the stochastic process of quasiparticle poisoning. An analogous line broadening effect upon atomic transitions from random telegraph-type resonance fluctuations has been analyzed elsewhere⁷⁸. With the CPB biased at $n_g \cong 0.063$, a small fraction of gate charge is modulated by the nanomechanical motion according to

$\delta n_g = ((\partial C_G / \partial x) V_N / 2e)x$, which results in modulation of γ and ω_0 . Assuming that

the equation of motion takes the form,

$$m\ddot{x} + m\left(\gamma + \frac{\partial\gamma}{\partial x}x + \frac{1}{2}\frac{\partial^2\gamma}{\partial x^2}x^2\right)\dot{x} + m(\omega_0^2 + 2\omega_0\frac{\partial\omega_0}{\partial x}x + \omega_0\frac{\partial^2\omega_0}{\partial x^2}x^2)x = f$$

up to second order in x , we can identify higher order terms such as $m(\partial\gamma/\partial x)x\dot{x}$,

$m(\partial^2\gamma/\partial x^2)x^2\dot{x}/2$, and $2m\omega_0(\partial\omega_0/\partial x)x^2$, and collect them following Lifshitz et. al.⁷³

Following this approach, the nonlinear dissipation coefficient is then given by,

$$\eta = \frac{m}{2}\frac{\partial^2\gamma}{\partial x^2} - \frac{2m}{\omega_0}\left(\frac{\partial\gamma}{\partial x}\right)\left(\frac{\partial\omega_0}{\partial x}\right) = \left(\frac{k_{eff}}{2\omega_0^2}\frac{\partial^2\gamma}{\partial n_g^2} - \frac{2k_{eff}}{\omega_0^3}\frac{\partial\gamma}{\partial n_g}\frac{\partial\omega_0}{\partial n_g}\right)\left(\frac{\partial n_g}{\partial x}\right)^2.$$

From the measured resonance linewidth vs. gate charge in Fig. 14, we obtain

$\partial^2\gamma/\partial n_g^2 \approx 5 \times 10^5 s^{-1}$, $\partial\gamma/\partial n_g \approx -6 \times 10^4 s^{-1}$. From the resonance shift data, we have

$\partial\omega_0/\partial n_g \approx 1 \times 10^4 s^{-1}$, $\partial n_g/\partial x \approx 3.3 \times 10^9 m^{-1}$. Together these allow us to deduce

$\eta \cong 1 \times 10^9 (kg/m^2s)$. Employing the fluctuation-dissipation theorem, one expects this

nonlinear dissipation to be accompanied by displacement-dependent terms in the

nanoresonator's force noise correlation⁷⁵. This avenue has not been pursued in the current

experiment.

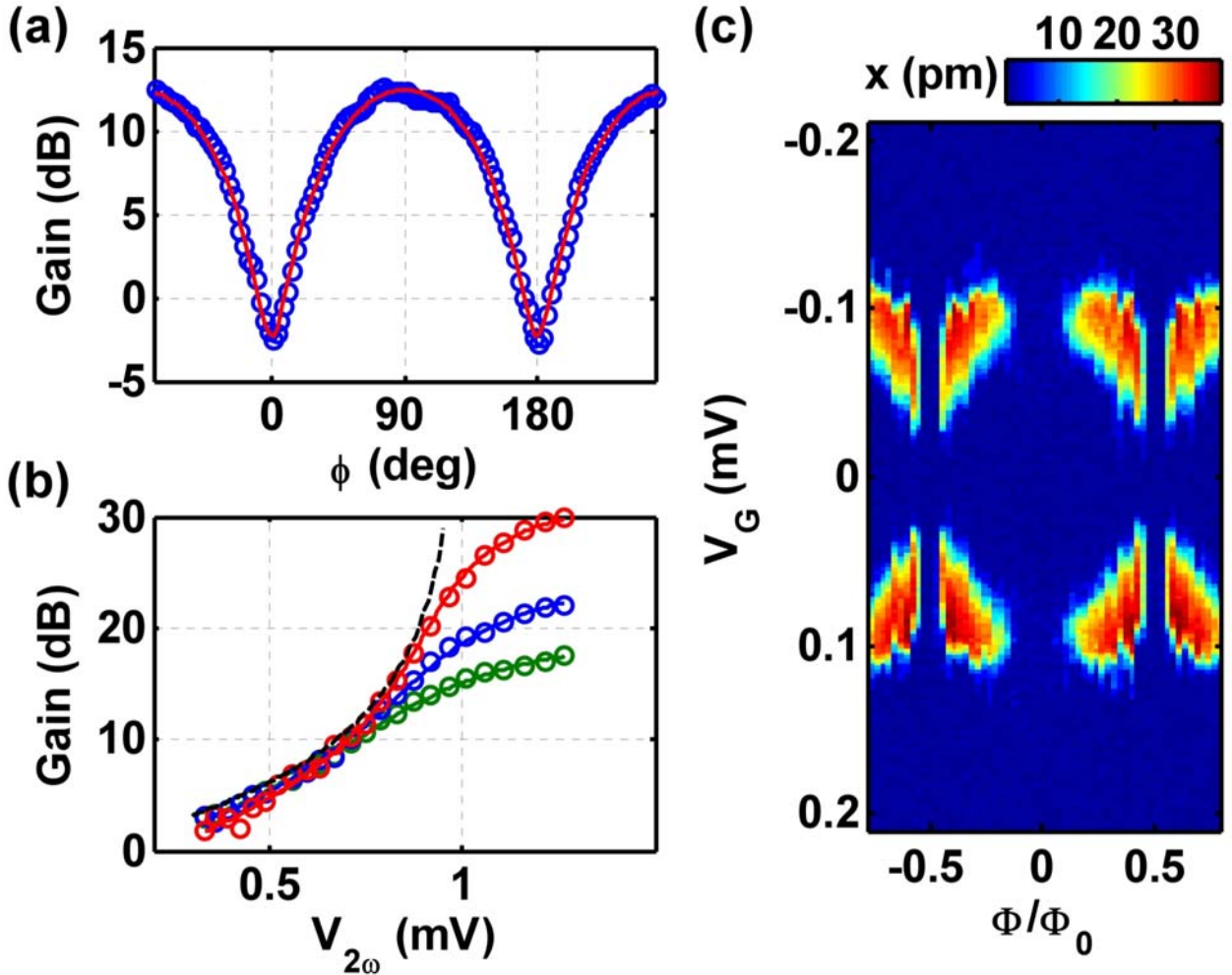


Figure 13: Mechanical parametric amplification and oscillation by driven qubit

(a) Parametric gain vs. phase of the resonator excitation. The blue circles are data taken at $V_{2\omega}=0.8$ mV and the red line is a fit to Eq. 7. The amplitude is normalized by the amplitude when $V_{2\omega}=0$ V and is expressed in dB. (b) Parametric gain vs. pump amplitude. From top to bottom, the circles correspond to the measured gains with $V_{\omega}=3.6$ nV, 6.3nV, 11nV. The black dashed line is a fit to Eq. 7 with $\phi = \pi/2$. The solid lines over circles are the fits to Eq. 8. (c) Map of the parametrically driven resonator amplitude with

$V_{\omega} = 0V$ and $V_{2\omega} = 1.6mV$, demonstrating self-oscillation in regions of CPB parameter space where the parametric response is maximum

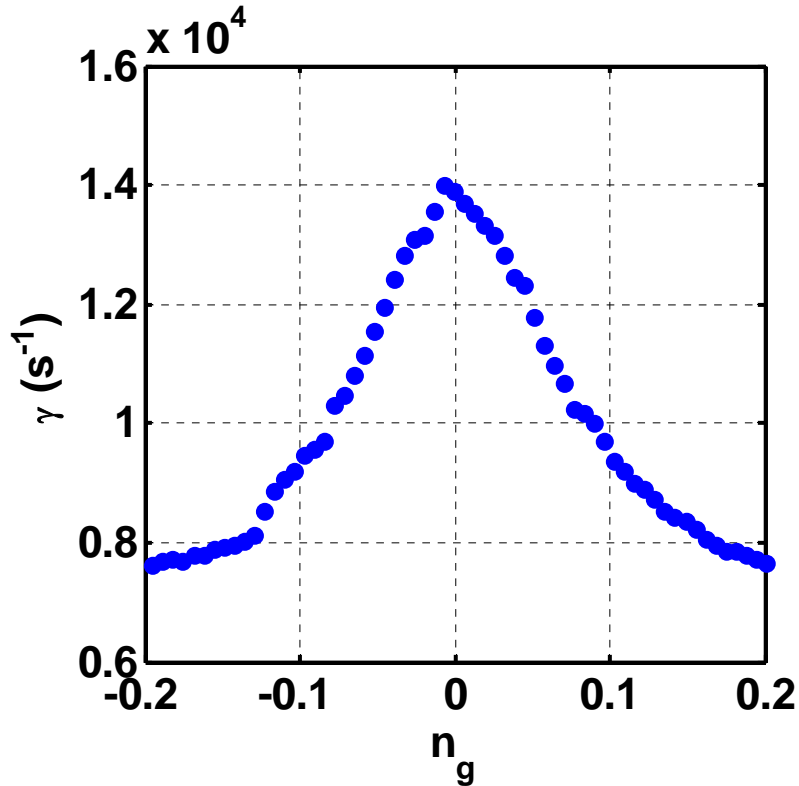


Figure 14: Nanomechanical resonance width vs. gate charge

3.2.3 Noise squeezing

The phase dependence of the amplification process in a degenerate parametric amplifier can be utilized to de-amplify one quadrature component of the input signal and reduce, or “squeeze”, the noise that accompanies the signal in that quadrature⁶⁴. We demonstrate this effect using our qubit-based parametric amplifier in degenerate mode to squeeze the

back-action noise emanating from the capacitive detection circuit. This excess back-action is due to input voltage noise of our cryogenic amplifier (noise temperature ~ 30 K). With the pump and drive voltage turned off, these voltage fluctuations drive the nanoresonator out of equilibrium with the thermal environment at 130 mK to an effective temperature about 8K. This value is extracted from the peak height ($S_{x,BA}$) of noise spectrum in Fig. 15a. With the pump on, we observe the squeezing effect using an RF lock-in to monitor both quadratures of the nanoresonator's motion as a function of the reference phase φ , Fig. 15b. De-amplification of each quadrature occurs with the expected $\pi/2$ phase difference between quadratures and yields maximum squeezing of 4 dB.

We start with the parametric pump set to zero, and the total displacement noise spectrum $S_x = S_{x,ADD} + S_{x,BA}$ is recorded for each of quadratures (X and Y) of lock-in. The two noise spectra show equivalent peak heights and noise floor levels, as expected. We choose X quadrature data to plot in Fig. 15a and to estimate $S_{x,ADD}$. The noise floor has a slope due to slight offset of LC matching circuit resonance and mechanical resonance. Accordingly, it is fit by a quadratic polynomial to obtain the noise density at the mechanical resonance, which is $S_{x,ADD}$ (Fig.16). With the parametric pump turned on,

the phase of the resonator excitation is swept, while S_x at the mechanical resonance is monitored. Following this procedure, $S_{x,BA} = S_x - S_{x,ADD}$ gives us the back-action noise for each phase. Figure 15b shows that the back-action noise from the amplifier is squeezed. To provide a detailed fit to this behavior, the nanoresonator biased at

$$V_{dc} = V_N - V_{NG} \text{ at its resonance is modeled as a resistor } (R_m = \frac{k_{eff}}{G\omega_0 Q} / \left(\frac{\partial C_{NG}}{\partial x} V_{dc} \right)^2)^{47}.$$

The impedance matching circuit transforms the impedance as $N^2:1$, where $N = \omega_T L_T / Z_0 \cong 50$ and $\omega_T = 1/\sqrt{L_T C_T}$. The amplifier is modeled as having two uncorrelated noise sources⁷⁹ (Fig. 12a); the spectral densities of these voltage and current noise sources are S_V, S_I , and an input impedance $Z_{in} = Z_0 = 50\Omega$ is assumed. In our set-up, $R_m \cong 0.8M\Omega$ for $G=1$ and $R_m / N^2 \gg Z_{in}$. The mechanical displacement is proportional to the current through Z_{in} , thus the noise current through Z_{in} gives the displacement noise. The spectral density of noise current through Z_{in} is,

$$S_{I,Zin} = \frac{S_V}{(R_m / N^2 + Z_{in})^2} + S_I \left(\frac{R_m / N^2}{R_m / N^2 + Z_{in}} \right)^2 \cong \frac{S_V}{(R_m / N^2)^2} + S_I.$$

We see the second term does not depend on the mechanical resonator and it is simply an additive contribution from the amplifier. The first term, by contrast, increases when R_m decreases; i.e., the coupling to the amplifier increases. Through this approach we identify the amplifier back-action noise as

$$S_{x,BA} = S_V / (R_m / N^2)^2 / (N\omega_0 V_{dc} (\partial C_{NG} / \partial x))^2 = S_V (GNQV_{dc} (\partial C_{NG} / \partial x) / k_{eff})^2$$

and the additive noise as

$$S_{x,ADD} = S_I / (N\omega_0 V_{dc} (\partial C_{NG} / \partial x))^2 .$$

It is evident that only the back-action noise is amplified or squeezed depending on the parametric gain G . And also, since only $S_{x,BA}$ depends on the mechanical Q , the noise floor under the motional peak of the displacement noise spectrum is $S_{x,ADD}$.

The total displacement noise is,

$$S_x = S_{x,BA} + S_{x,ADD} \cong S_V \left(\frac{GNQV_{dc} (\partial C_{NG} / \partial x)}{k_{eff}} \right)^2 + \frac{S_I}{(N\omega_0 V_{dc} (\partial C_{NG} / \partial x))^2} .$$

Here we do not include the thermomechanical noise of the nanoresonator since the noise temperature of the amplifier (~ 30 K) is much higher than the sample temperature. The displacement noise S_x at the nanomechanical resonance $\omega = \omega_0$ gives the measurement force noise, by $S_f = (k_{eff} / GQ)^2 S_x$. Thus the portion of force noise due to the amplifier is,

$$\begin{aligned} S_f &= \left(NV_{dc} \frac{\partial C_{NG}}{\partial x} \right)^2 S_V + \left(\frac{k_{eff}}{NGQ\omega_0 V_{dc} (\partial C_{NG} / \partial x)} \right)^2 S_I . \\ &= S_{f,BA} + S_{f,ADD} \end{aligned}$$

This is minimized when

$$S_{f,BA} = S_{f,ADD} \quad \text{or} \quad R_n \equiv \sqrt{S_V / S_I} = R_m / N^2,$$

and this relation gives the noise matching condition. The minimum force noise is then,

$$\min(S_f) = \frac{2k_{eff}}{G\omega_0 Q} \sqrt{S_V S_I} = \frac{4k_{eff} k_B T_N}{G\omega_0 Q}$$

where k_B is the Boltzmann constant and T_N is the minimum noise temperature of the amplifier.

From the measured $S_{x,ADD}$ and $S_{x,BA}$, we calculate S_V and S_I and get $S_V^{1/2} = 360 \text{ pV/Hz}^{1/2}$ and $S_I^{1/2} = 2.2 \text{ pA/Hz}^{1/2}$, which are close to what we measured in a separate measurement on the cryogenic amplifier, $S_V^{1/2} = 340 \text{ pV/Hz}^{1/2}$ and $S_I^{1/2} = 2.2 \text{ pA/Hz}^{1/2}$. Also, we extract the force sensitivity $83 \text{ aN/Hz}^{1/2}$ with no parametric gain. Comparing this with the expected thermomechanical noise force, $\sqrt{4k_{eff} k_B T / (\omega_0 Q)} = 5.1 \text{ aN/Hz}^{1/2}$, we see the preamplifier noise is dominant, and the parametric amplification indeed improves the force sensitivity, and it also confirms the validity of the assumption neglecting the thermomechanical noise.

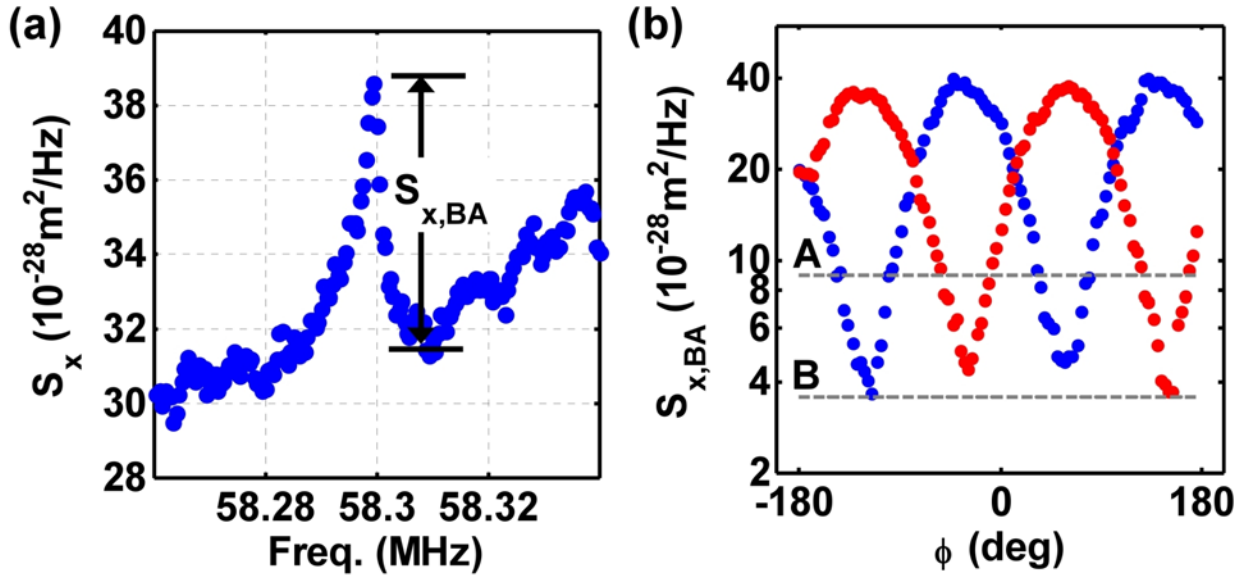


Figure 15: Amplifier back-action noise squeezing

(a) The noise spectral density of the mechanical displacement with no parametric gain.

The slope in the background is due to a slight offset of the nanomechanical resonance from the LC matching frequency. (b) Back-action noise vs. reference phase. (blue) X-quadrature of the lock-in. (red) Y-quadrature. Line “A” is the noise level with no parametric gain and line “B” is at -4 dB from noise level “A”.

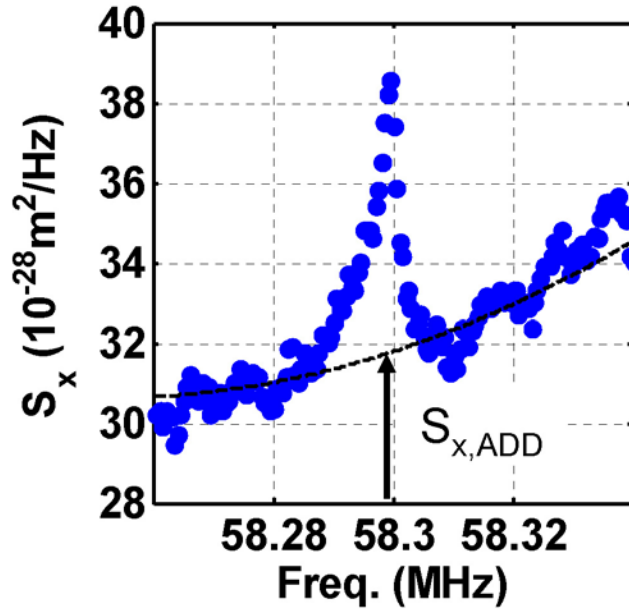


Figure 16: Displacement measurement noise floor estimate

3.3 Discussion

We have demonstrated parametric amplification of nanomechanical motion using the nonlinearity of a driven CPB qubit. The dispersive nanomechanical resonance shift provides a parametric pumping mechanism that is significantly more efficient than existing techniques for parametric nanomechanical modulation. Our proof-of-principle experiment shows that this parametric effect can be used to squeeze nanomechanical motion. Integrating a superconducting microwave resonator with this system should enable the preparation and observation of quantum squeezed states and superposition states of the mechanics.

To the best of our knowledge, this qubit-based amplification and squeezing technique is the first demonstration of the use of a qubit as an auxiliary system to manipulate the state of nanomechanical motion. In this first demonstration we manipulate motion in the classical regime. In future experiments, quantum state engineering of the mechanics will be possible by replacing the present capacitive read-out circuit with a low-loss superconducting microwave resonator (SWR). Through capacitive coupling of each element to the nanoresonator, independent manipulation of either the qubit and SWR, or simultaneous manipulation of both, could then be used to tailor a specific nanoresonator Hamiltonian⁷⁰. This could enable the production of a large variety of quantum states, including vacuum squeezed states and superposition states.

Generating such states will require reducing the thermal occupation number N of the nanomechanical mode to a value that is close to its quantum ground state (i.e., $k_B T < \hbar \omega_0$). Attainment of the quantum ground state of a 6 GHz micro-mechanical resonator was recently demonstrated using conventional dilution refrigeration¹¹. Also, for a nanoresonator similar to what is described in this paper, $N=3.8$ has been reached using dynamical back-action cooling from a SWR⁶⁶. With a nanoresonator cooled to low

occupation numbers, a vacuum squeezed state of the mechanics could be prepared by utilizing the qubit squeezing technique demonstrated here. Subsequent operations on the qubit applied through a series of microwave pulses could then be used to engineer the nanoresonator interaction Hamiltonian $g(\hat{a}^\dagger \hat{a})^2$ and generate a superposition of the squeezed states⁷⁰. Implementation of this type of superposition protocol will require nanoresonator interaction strength, g , that exceeds both the qubit damping, γ , and nanoresonator damping, Γ . For the present sample we estimate $g \cong 2$ kHz, $\Gamma = 1.1$ kHz, and $\gamma \cong 1$ GHz⁷². Modifications to the geometry of the sample should yield a factor of 10, or more, increase in the electrostatic coupling λ . This could yield a coupling strength, $g \cong 200$ kHz, which approaches the lower limit of qubit damping rates demonstrated in circuit-QED, $\gamma < 1$ MHz²⁴.

Chapter 4

Cooling of a nanomechanical mode with a microwave resonator

The ground state of a quantum harmonic oscillator has the lowest possible energy and the minimum uncertainty in displacement, or “zero point motion”, with r.m.s. amplitude $x_{zp} = \sqrt{\hbar/2m\omega}$. This is one of the signatures of its quantum nature that makes it distinct from classical physics. It also provides a useful starting point for generating other interesting quantum states⁸⁰ such as squeezed states, superposition states, and number states. A mechanical resonator can be placed in its ground state, in principle, simply by lowering its temperature below $\hbar\omega/k_B$. For resonance frequencies in the GHz range, conventional dilution refrigeration can provide access to low enough temperatures ($\hbar/k_B = 48 \text{ mK/1GHz}$). A recent demonstration of the cooling of a micro-mechanical resonator to the ground state was done in this way¹¹. For lower frequency devices, opto-mechanical coupling provides a possible option for optical sideband cooling^{81, 82}. By coupling the mechanical and optical degrees of freedom to modulate the resonance frequency of an optical cavity, and by driving the cavity with light detuned from the

cavity resonance, the anti-Stokes scattering of the cavity photon absorbs mechanical quanta, which cools the mechanical mode. For different cavity geometries and coupling schemes, mechanical occupation factors in the range of 30 to 60 quanta have been demonstrated⁸³⁻⁸⁵.

In the present work, a coplanar waveguide microwave resonator capacitively coupled to a nanomechanical resonator is studied^{66, 86}. This system has the same cooling physics as optical back-action cooling, but allows for a more convenient implementation of dilution refrigeration. The coupling between the microwave field and the mechanical displacement is here enhanced compared to that of previous work⁶⁶. This is achieved by using a higher frequency microwave resonator, reaching 5 times optical damping rate. For this system we predict that the mechanical resonator should reach the ground state. However, in carrying out our experiments we encountered unexpected heating in addition to the optical cooling. This served to keep the mechanical resonator at a minimum observable occupation number of 7.5 quanta.

The heating we have observed is consistent with a model of two-level systems resonantly coupled to the mechanical mode. This model predicts a 1/2-power law between the bath

heating rate and the observed mode occupation number. This effect underscores the need for further studies on characterizing and reducing the fluctuations from the ubiquitous two-level system bath, to allow attainment of the quantum ground state in nanomechanical resonators.

4.1 Theory

4.1.1 Superconducting coplanar waveguide resonator

The coplanar waveguide (CPW) is a type of transmission line with two ground planes symmetrically placed about a center conductor in a planar geometry⁸⁷ (Fig. 17a). An open-circuit section of CPW acts a half-wave microwave resonator. An equivalent circuit for such a resonator can be modeled with a parallel resistance R , capacitance C , and inductance L . Their equivalent values can be derived by considering the input impedance around the resonance frequency (Fig. 17c)⁸⁷,

$$R = Z_c / (\alpha l), C = \pi / (2\omega_0 Z_c), L = 1 / (\omega_0^2 C) \quad (\text{Eq. 8}).$$

Here the intrinsic quality factor is $Q_{\text{int}} = \omega_0 RC$, α is the attenuation per unit length, ω_0 is the resonance frequency, Z_c is the characteristic impedance of the transmission line, and l is the resonator length. By using a superconducting metal as the conductor, the intrinsic loss can be made very low²², even reaching $Q_{\text{int}} > 10^6$, making it useful for

sensitive detection of the mechanical motion. Coupling to the open-circuit CPW resonator with input and output capacitors as shown in Fig 17c, the resonant response S_{21} is measured. The coupling adds dissipation due to the loss to the outside loads, and the input/output quality factor due to loading is given by $Q_{in/out} = C/(\omega_0 C_{in/out}^2 Z_0)^{87}$. The total Q is given by $1/Q_{tot} = 1/Q_{int} + 1/Q_{in} + 1/Q_{out}$. The quality factors give the damping rate as $\kappa = \omega_0 / Q$.

From the circuit model, the electromagnetic energy stored in the resonator when the resonator is driven by a input power P_{in} at ω_R is,

$$U = P_{in}(\omega_R) \frac{\kappa_{in}}{(\omega_R - \omega_0)^2 + (\kappa_{tot}/2)^2} \quad (\text{Eq. 9}).$$

This defines the number of photons, $n_p = U/(\hbar\omega_0)$ and the output power, $P_{out} = U\kappa_{out}$.

4.1.2 Back-action cooling of mechanical motion

The nanomechanical motion modulates the capacitance of the CPW resonator. This couples the microwave field and the nanomechanical displacement, $g = \partial\omega_0 / \partial x = (\omega_0 / 2C)(\partial C_g / \partial x)$. Here C_g is the gate capacitance between the mechanical resonator and the CPW resonator (Fig. 17b). With the CPW resonator driven by a red-detuned tone $\omega_R (< \omega_0)$, the energy in the microwave resonator is modulated

with the mechanical motion; this generates a force on the mechanical resonator. Since the force has a time-lag corresponding to the ring-down time of the CPW resonator, there is net work done by the mechanical resonator, thus additional opto-mechanical damping γ_{opt} arises. The effective mode temperature of the mechanical resonator is given classically by $T_{eff} = T_0 \gamma_m / (\gamma_m + \gamma_{opt})$, where T_0 is the initial temperature without microwave power.⁸⁸

This process also can be analyzed with a quantum noise approach, and the cooling can be viewed as absorption of the mechanical energy by the CPW resonator via anti-Stokes scattering of microwave photons⁸¹. In this case, the coupling up-converts red-detuned microwave photons by absorbing mechanical energy. Since the rate of this up-conversion process is proportional to the density of final states, it is maximized at $\omega_R = \omega_0 - \omega_m$.

The resulting damping rate is⁸¹

$$\gamma_{opt} = \frac{4g^2 x_{zp}^2}{\kappa} n_p \frac{1}{1 + (\kappa/4\omega_m)^2} \cong \frac{4g^2 x_{zp}^2}{\kappa} n_p \quad (\text{Eq. 10}).$$

Here x_{zp} is the zero-point motion of the mechanical resonator, κ is the CPW resonance linewidth, n_p is the mean number of microwave pump photons, and the sideband-resolved limit $\kappa/4\omega_m \ll 1$ is assumed. The total linewidth of the mechanical

resonance is then

$$\gamma_m = \gamma_{m0} + \gamma_{opt}$$

where γ_{m0} is the intrinsic mechanical resonance linewidth with no microwave back-action broadening.

From the detailed balance equation, the total number of mechanical quanta is given by

$$n_m = \frac{\dot{n}_{m,bath} + \gamma_{opt} n_c}{\gamma_{m0} + \gamma_{opt}} \quad (\text{Eq. 11})$$

where $\dot{n}_{m,bath}$ is the mechanical mode heating rate from the environment, and $n_c = (\kappa/4\omega_m)^2 + n_{c0}(1 + 2(\kappa/4\omega_m)^2)$ where n_{c0} is the occupation number of the CPW resonator. The lowest possible mechanical occupation is n_c , and ground state cooling of the mechanical mode is only possible in the sideband-resolved limit when $\kappa/4\omega_m < 1$, and also $n_{c0} \ll 1$. In practice, the microwave resonator acts as an additional dissipative bath, at a temperature of $\hbar\omega_m n_c / k_B$, coupled to the mechanical mode with damping rate γ_{opt} .

4.2 Experimental Setup

4.2.1 Device parameters

$\omega_m / 2\pi = 7.2 \text{ MHz}$	Nanomechanical resonance frequency
$m_{eff} \cong 2 \text{ pg}$	Estimate of the nanomechanical resonator mass deduced from the geometry measured with scanning electron micrograph and known material density
$x_{zp} \cong 24 \text{ fm}$	Zero-point motion of the nanomechanical resonator ($x_{zp} = \sqrt{\hbar / 2\omega_m m_{eff}}$)
$\omega_0 / 2\pi = 11.8 \text{ GHz}$	CPW resonator resonance frequency
$\kappa / 2\pi = 500\text{--}600 \text{ kHz}$	CPW resonator linewidth. Varies with applied microwave power
$g / 2\pi \cong 180 \text{ kHz}$	Coupling $\partial\omega_0 / \partial x$ measured at 300 mK with calibrated cryogenic coaxial cables

4.2.2 Cryogenic circuit

From the room temperature SMA connector for the microwave input, UT-141 CuNi coaxial cable is used down to the 4 K stage, where a 10 dB attenuator is located. From the 4 K stage to the mixing chamber, attenuators are employed as following: 3 dB at the 1 K plate, 6 dB at the still, and 11 dB at the cold plate, connected with UT-34 BeCu coaxial

cable. The attenuators are wrapped with copper foil and bolted down to ensure good thermal contact. The end of the input line is connected to the sample case, and the output of the sample case goes into two cryogenic isolators in series, which provides more than 40 dB of total isolation. A UT-85 niobium coaxial cable is used to connect the isolators to the input of the cryogenic HEMT amplifier, and the amplifier output is connected to a UT-141 CuNi cable, which goes to the top of the fridge.

4.2.3 Room temperature circuit

A microwave filter based on the whispering gallery mode of a pair of sapphire cylinders is used to filter the phase noise of the microwave source (Appendix E). The measured isolation is 23 dB at the CPW resonance frequency. After the cryogenic HEMT amplifier, a room temperature low noise amplifier is used as preamplifier before the spectrum analyzer.

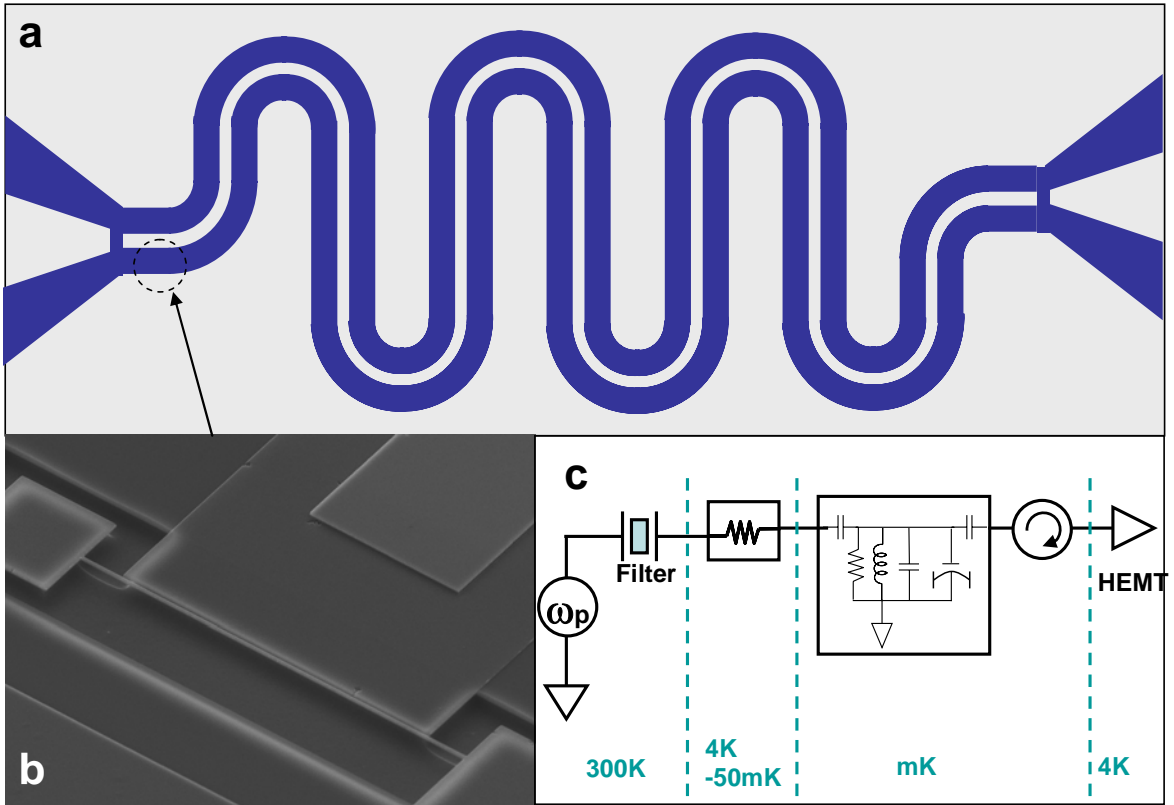


Figure 17: Sample picture and measurement schematic

(a) Schematic of the microwave coplanar waveguide resonator. A half-wavelength section of waveguide is coupled through the input and output capacitances from the tapered ports. The substrate has 100nm of low stress silicon nitride on high-resistivity silicon. Sputtered niobium is used as the metal layer. At the voltage antinode of the fundamental resonance at 11.8 GHz, (dotted circle), a nanoscale suspended beam is connected to the ground plane, and capacitively coupled to the center conductor of the microwave resonator. (b) Nanomechanical resonator. It is etched and suspended from the substrate using an aluminum layer as a mask, which also serves as conducting layer to couple the

mechanical mode to the microwave field. The dimensions are, $20 \mu\text{m} \times 150 \text{ nm} \times 160 \text{ nm}$ (LxWxT), where the thickness is composed of 80 nm Al and 80 nm SiN. The fundamental resonance is at 7.5 MHz, and the 2nd resonance is at 15.5 MHz. (c) Measurement circuit. A microwave tone at the frequency ω_p is applied through the whispering-gallery-mode sapphire filter. After cold attenuators which attenuate the room temperature black-body radiation, the signal propagates through the microwave resonator, and is amplified by the cryogenic high electron mobility transistor (HEMT) amplifier. Two cryogenic circulators are used to isolate the noise emanating from the 4K amplifier.

4.3 Results

4.3.1 Thermomechanical noise

With low microwave power, the upconverted microwave power from ω_R to ω_0 shows up as the thermomechanical noise peak, and is measured at different bath temperatures (Fig. 18a). For a small mechanical displacement x , substituting $C = C_0 + (\partial C_g / \partial x)x$ into the RLC circuit model (Section 4.1.1), and collecting internal voltage terms oscillating at $\omega = \omega_R + \omega_m$ yields⁸⁹,

$$P_{mech} = P_{out} (g / \kappa)^2 \cdot 2 \langle x^2 \rangle \quad (\text{Eq. 12}).$$

This gives the calibration of the mechanical occupation number vs. measured area based

upon the equipartition theorem, $\frac{1}{2}m_{eff}\omega_m^2 \langle x^2 \rangle = \frac{1}{2}k_B T_{bath}$. Due to changes in κ for different temperatures, a linear fit between $P_{mech} \cdot \kappa^2$ and bath temperature is done, giving $(3.5 \pm 0.1) \cdot 10^{-3} [\text{fW} \cdot \text{MHz}^2]$ per mechanical quanta at $n_p = 1.1 \cdot 10^4$. Below 40 mK, increasing scatter is observed in the deduced noise power. This scatter becomes much more prominent with the use of a cryogenic bias-tee (Anritsu K250) (Fig. 18b). A possible reason for this increased scatter could be the ferromagnetic material inside the bias-tee; these kinds of materials show anomalously high heat capacity at low temperatures. We discontinued using the bias-tee in subsequent measurements, but this complication will need to be investigated more carefully for different set-ups where the bias-tee is necessary.

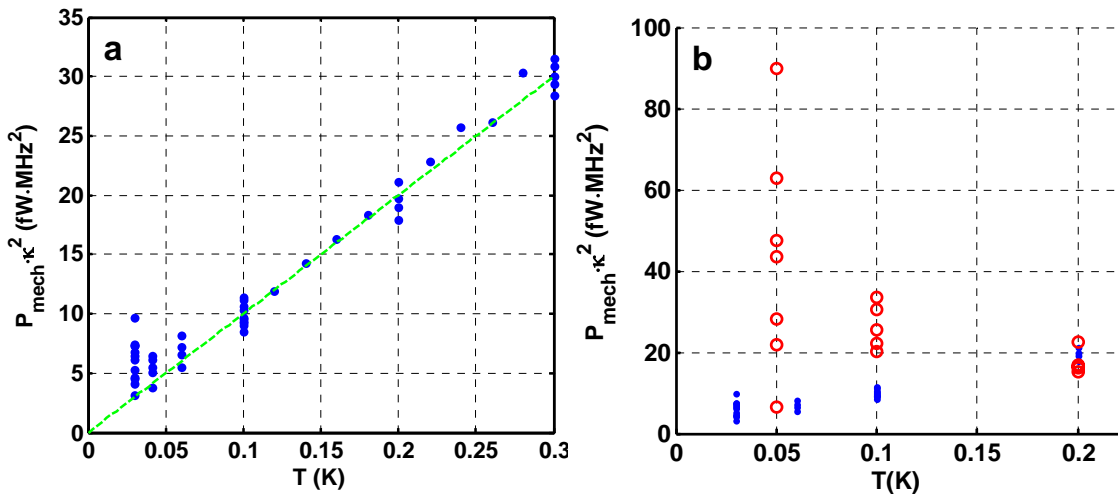


Figure 18: Thermomechanical noise power vs. bath temperature

(a) Measured noise power without bias tee in the circuit. Blue dots correspond to each

Lorentzian fit result. Data falls on a line crossing zero (green line), indicating the mechanical mode follows the bath temperature and obeys the equipartition theorem. (b) noise power with bias tee (red circles). Blue dots are a subset of data in (a), overlaid as reference. Below 100 mK, the bias tee creates force noise and drive the nanoresonator, resulting large variations in the thermomechanical noise power.

4.3.2 Back-action cooling of mechanical motion

To avoid the excess scatter, we set the fridge temperature at 50 mK, which is above the temperature where the thermomechanical noise begins to diverge. By applying higher microwave power, the linewidth broadening of the mechanical noise peak is observed as in Fig. 19a, fitting well with Eq. 10. The thermal calibration in shown Fig 18 gives the number of mechanical quanta from the measured noise power $P_{mech} \cdot \kappa^2$. In the limit where the CPW resonator has no noise (shot noise, source phase noise, etc.), we simply have $n_m \propto P_{mech} \cdot \kappa^2$. However, in the presence of noise, the fluctuation in the microwave field generates a down-converted force by mixing with the pump tone at ω_R . A detailed calculation based on input-output theory gives the output spectrum from the CPW resonator⁶⁶,

$$S(\delta) = 1 + \frac{4\kappa_{out}}{\kappa_{tot}} n_c + \frac{4\kappa_{out}}{\kappa_{tot}} \frac{\gamma_{opt}\gamma_m}{\delta^2 + (\gamma_m/2)^2} n_{eff}.$$

Here δ is the detuning of the measurement frequency from ω_0 , n_c is the occupation number of the microwave field in the CPW resonator and $n_{eff} = n_m - 2n_c$. n_c is measured by measuring the total noise power under the CPW resonance peak. To crudely calibrate this noise power, we employ the known noise temperature (6.5 K) of the HEMT amplifier in concert with the 1.5 dB attenuation between the sample and the amplifier (measured separately at 4 K). The measured n_c is plotted in Fig. 19b, showing close to 1/2-power law behavior. This is consistent with measurements of similar superconducting resonators, where phase noise $\delta\omega_0 / \omega_0 \sim n_p^{-1/2}$ has been observed^{90,91}. This excess noise is attributed to two-level systems resonantly interacting with the microwave field. The measured linewidth also follows the prediction of two-level system theory^{90,92}, showing the saturation of dissipation at high microwave power.

$$\kappa = \frac{\kappa_{TLS}}{\sqrt{1 + n_p / n_{crit}}} + \kappa_0 \quad (\text{Eq.13}).$$

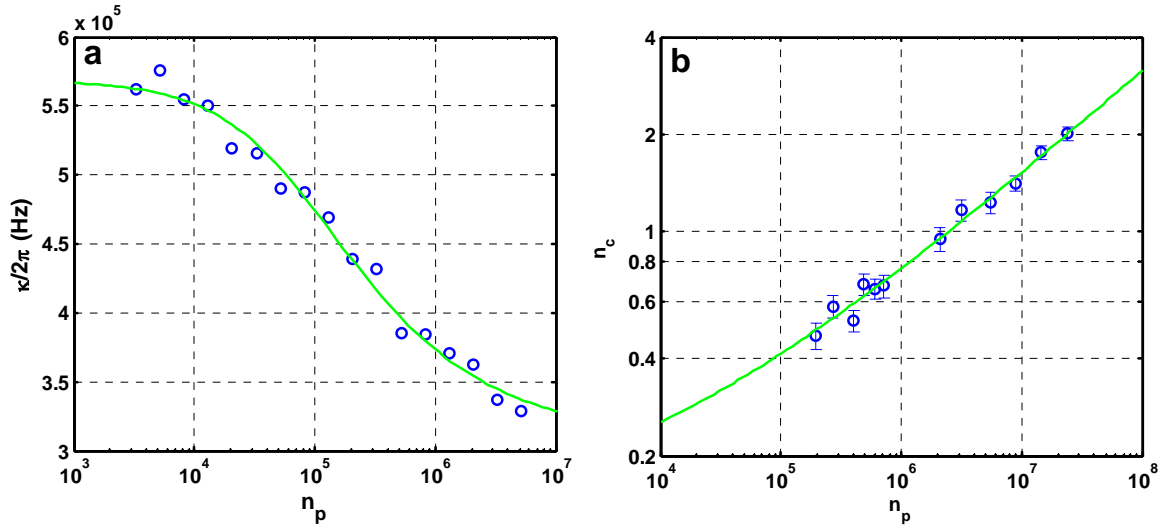


Figure 19: CPW resonator loss due to two-level systems

(a) CPW resonator linewidth. Green line is a fit to Eq. 13. (b) The noise power from the microwave resonator plotted in number of quanta. Green line is a power-law fit, $n_c \cong 6 \cdot 10^{-3} n_p^{0.33} + 0.1$, showing close to square-root dependence which has been observed in similar coplanar resonators.

The lowest n_m we are able to observe is 7.5 ± 0.8 . (Fig. 19b) This is significantly higher than $n_m \sim 2$ that is expected from the highest $n_c \cong 2$ and Eq. 11. The blue dashed line in Fig. 19b, displaying what is expected from the assumption of constant $\dot{n}_{m,bath} = n_{m0} \gamma_{m0}$, where $n_{m0} = 1/(e^{h\omega_m/k_B T} - 1) = 144$ and $\gamma_{m0} = 28$ Hz, shows a large discrepancy with data.

From this we conclude that there are other sources of heating involved.

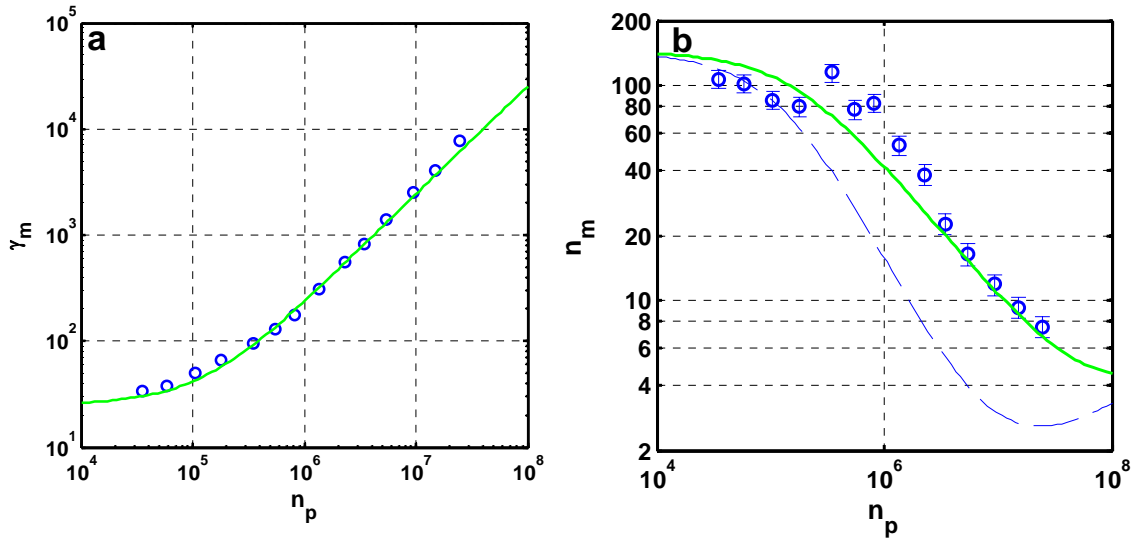


Figure 20: Back-action cooling of mechanical motion

(a) Linewidth and (b) mean occupation of nanomechanical resonator vs. number of microwave photons in the CPW resonator. (a) Green line is a fit to Eq. 10 (b) Dashed blue line is calculated from Eq. 11, assuming constant $\dot{n}_{m,bath}$. Green line is calculated with two-level bath model (described in Fig. 21).

One possible explanation for this excess heating is coupling to a bath of two-level fluctuators. As in the case of CPW microwave resonator, the mechanical resonator might be coupled to such a bath via the strain field⁹². In bulk systems, studies on ultrasonic attenuation and sound velocity at low temperatures show such effects⁹³⁻⁹⁵. As with the electromagnetic case (Eq. 13), resonant interaction of two-level systems with the phonon field also shows saturation effects in the dissipation⁹⁴,

$$\frac{1}{Q_{TLS}} = \frac{\pi N_a M^2 \tanh(\hbar\omega_{TLS}/2k_B T_{TLS})}{\rho v^2 \sqrt{1+I/I_c}} \quad (\text{Eq.14}).$$

Here N_a is the density of states of two level systems per unit volume ($\text{J}^{-1}\text{m}^{-3}$), M is the coupling between two-level system and strain ($\partial(\text{energy})/\partial(\text{strain})$), ρ is the mass density, v : speed of sound, and I_c is the critical acoustic intensity ($= \hbar^2 \rho v^3 / (2M^2 T_1 T_2)$).

According to this picture, two-level systems resonantly coupled with the nanomechanical mode $\omega_{TLS} \cong \omega_m$ will lead to heating, which is given as

$$\dot{n}_{m,TLS} \cong \frac{k_B T_{TLS}}{\hbar \omega_m} \frac{\omega_m}{Q_{TLS}} \cong \frac{\pi N_a M^2}{2 \rho v^2} \frac{\omega_m}{\sqrt{1+n_m/n_{crit}}} \quad (\text{Eq.15})$$

in the limit of $\hbar\omega_{TLS}/k_B T_{TLS} \ll 1$. The total bath heating rate is then

$$\dot{n}_m = \dot{n}_{m0} + \dot{n}_{m,TLS},$$

where $\dot{n}_{m0} = n_{m0} \gamma_{m0}$ is the background heating rate with no coupling with two-level

baths. Fig. 21 shows the measured data at 50 mK and 300 mK with a fit to Eq. 15.

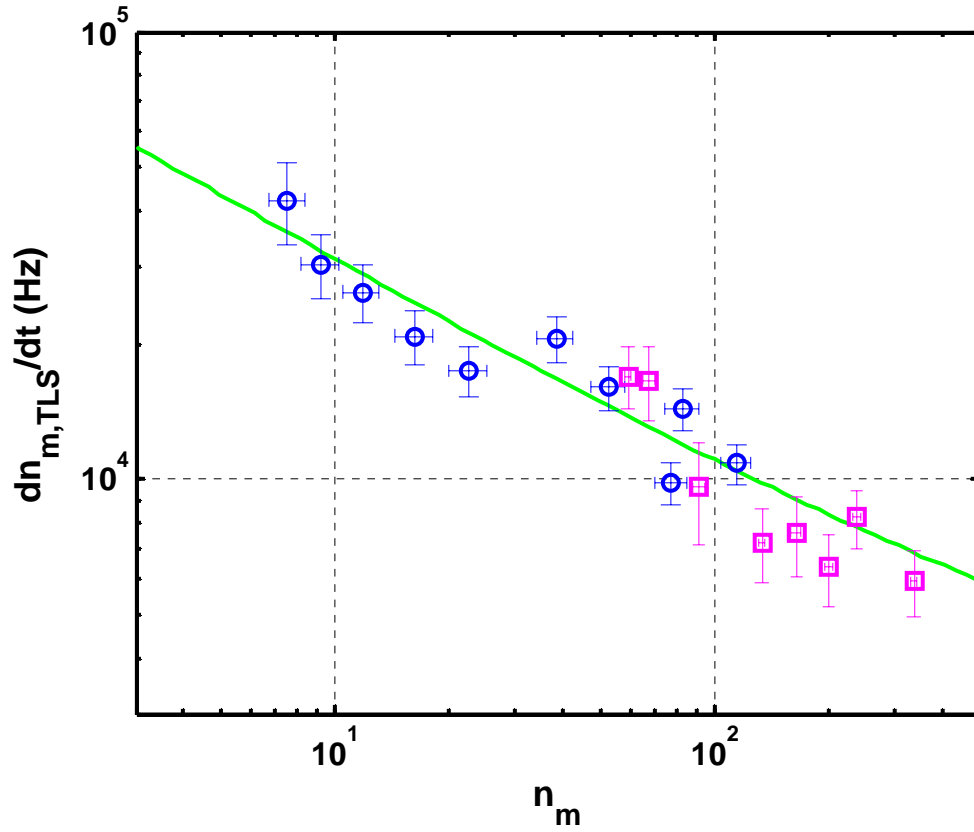


Figure 21: Heating rate from the two-level bath

(Blue circle) 50 mK data, (magenta square) 300 mK data. The green line is a fit of 50 mK data to the resonant two-level bath model, Eq. 15, yielding $\pi N_a M^2 / 2 \rho v^2 = 0.19$, $n_{crit} = 3.8 \cdot 10^{-3}$. The 300 mK data points also match the fit.

The fitted critical occupation number n_{crit} is consistent with an estimate based upon a bulk silicon oxide measurement. The critical intensity of Suprasil W at 480 mK and 750

MHz⁹³, 10^{-3} W/m^2 is scaled to SiN at 50 mK and 7.2 MHzⁱⁱ using the formula of relaxation time for one-phonon processes⁹⁶,

$$T_1^{-1} = \left(\frac{M^2}{v^5} \right) \frac{\omega^3}{2\pi\hbar\rho} \coth\left(\frac{\hbar\omega}{2k_B T} \right)$$

which is $I_c \approx 10^{-8} \text{ W/m}^2$; thus the critical occupation number is $n_{crit} \approx I_c \cdot (W \cdot T) / \omega_m / (\hbar\omega_m) \approx 10^{-3}$, which agrees with the fit result within an order of magnitude. The density of states of the two-level systems, $N_a = 3 \cdot 10^{48} \text{ J}^{-1} \text{ m}^{-3}$ ⁱⁱⁱ, means ~ 20 resonant two-level systems within the bandwidth $1/T_2$ at ω_m .

The same resonant interaction also gives logarithmic dependence in the resonance frequency^{92,94}. The measured $N_a = 3 \cdot 10^{45} \text{ J}^{-1} \text{ m}^{-3}$ is much smaller than the value above (Appendix D), but it should be noted that two values can disagree. Since the logarithmic dependence comes from the two-level systems with energy $E \approx k_B T_{bath}$, far from ω_m and not saturable, the two measurements probe different sets of two-level systems that, in general, will have different densities of states⁹². Also, both N_a are many orders of

ii Assumed ρ (Suprasil)=2200 kg/m³, v (Suprasil)=6000m/s, ρ (SiN)=3000 kg/m³, v (SiN)= 10^4 m/s, $T_2^{-1} \cong T_1^{-1} / 2$

iii Assumed $M \cong 0.4\text{eV}^{94}$, and $T_2 \cong 5\mu\text{s}$ which is from $I_c \approx 10^{-8} \text{ W/m}^2$ and $T_2^{-1} \cong T_1^{-1} / 2$

magnitude higher than bulk values⁹⁴. Perhaps this can be attributed to the high surface-volume ratio of the device, since the surface is believed to have a significantly increased density of two-level systems due to the micro-machining process⁹⁷.

4.4 Discussion

We have observed back-action cooling of a nanomechanical mode with a CPW microwave resonator down to occupation number of 7.5. At small mechanical occupation numbers, excess heating is revealed, which shows 1/2-power law behavior vs. mechanical occupation number. This is consistent with the model of two-level systems resonantly coupled to the mechanical resonator, and can be understood as the saturation of resonant two-level systems. The two-level bath model gives the maximum expected bath heating rate as $\sim 10^6$ Hz, which is equivalent to mechanical linewidth of about 7 kHz at 50 mK. This calls for much stronger back-action, $\gamma_{opt} \sim 1$ MHz, i.e. higher coupling $g \sim 2$ MHz to reach the ground state. A new geometry with larger coupling capacitance, for example, a planar structure with a small gap, might achieve this goal. Also, our results show that the mechanical resonator at ground state should have higher bath heating than is measured at higher occupation numbers. This discrepancy calls for more studies on reducing the two-level system density.

Chapter 5

Summary

Coupled dynamics between a nanomechanical resonator and superconducting quantum circuits have been studied in the three experiments of this thesis. The research presented is an effort toward realizing quantum states of the macroscopic mechanical systems, in the context of studying the quantum limit of force detection, and quantum coherence of macroscopic objects.

First, mechanical resonance shifts due to a dispersive interaction with a Cooper-pair box have been measured. The coupling strength is large enough to satisfy one of the conditions for a host of quantum nanomechanical measurements, such as non-demolition measurement of qubits²³ and preparation of motional quantum states^{27, 36, 70}. The microwave-driven response of the qubit has been measured using the dispersive shift as the probe. Rabi oscillations and Landau-Zener tunneling are observed, proving the coherence in the qubit dynamics.

Second, the dispersive shift has been used to parametrically excite nanomechanical motion. A degenerate parametric amplification and oscillation is demonstrated, with an observation that nonlinear dissipation which limits the maximum obtainable gain. The process also yields squeezing of the back-action noise of the detection amplifier, up to 4 dB. The efficiency of parametric excitation is 3000 times better than the prevailing technique of using geometric capacitance. It also provides the first demonstration of using the qubit as an auxiliary system to modify nanomechanical dynamics. With it we have elucidated a scheme for generation of nanomechanical quantum states, which will become possible with improvements in detection and initial preparation of mechanical states.

Third, a high-Q coplanar waveguide resonator has been capacitively coupled to nanomechanical motion. This yields a sensitive detection scheme, which allows the detection of displacement down to a few mechanical quanta. The back-action from microwave photons provides cooling of thermal nanomechanical motion. The thermal state with an average of 7.5 quanta is reached. This extremum appears to be limited by increased bath heating due to two-level systems resonant with the mechanical motion. This observation of additional heating suggests that efforts toward improving coupling

and reducing two-level system density will be important to reach the motional ground state via back-action cooling. With improvements in coupling and engineering of mechanical dissipation, motional ground states could be prepared, starting from thermal states. More elaborate quantum state manipulation, with superconducting qubits, could be employed, in order to generate and use these “mechanical” quantum states.

The results presented in this thesis show some of the possible routes toward macroscopic mechanical quantum states. In future, improvements in the quality of mechanical resonators and quantum circuit components are anticipated. Also, stronger coupling between these elements will be achieved. These ongoing efforts will help to reveal the connection between classical and quantum physics, and possibly could open the path to quantum engineering with macroscopic mechanical systems.

Appendix A

Nuclear orientation thermometry

Nuclear orientation thermometry works by the anisotropic gamma-ray emission of nuclei.

The emission probability depends on the polarization of nuclear magnetic moments,

which is a function of the Boltzmann distribution^{98, 99}. It is a primary thermometry

because the theory is well established, and it does not need extra calibrations except

normalization of counting rates at high temperatures.. For emission parallel to the

magnetic field, the probability for ⁶⁰Co is,

$$W(T) = 1 + 0.04333Q_2 \sum_{m=-2}^2 m^2 P(m) - 0.00333Q_4 \sum_{m=-4}^4 m^4 P(m)$$

where Q_n is geometry parameter normally close to 1 and $P(m)$ is the thermal

occupation of the nuclear state, $e^{-\varepsilon_m/k_B T} / \sum_{m=-J}^{+J} e^{-\varepsilon_m/k_B T}$, $\Delta\varepsilon_m/k_B = 6.0725$ mK for the

internal field of ⁶⁰Co single crystal. This magnetic energy scale limits its useful

temperature range to between 1–100 mK.

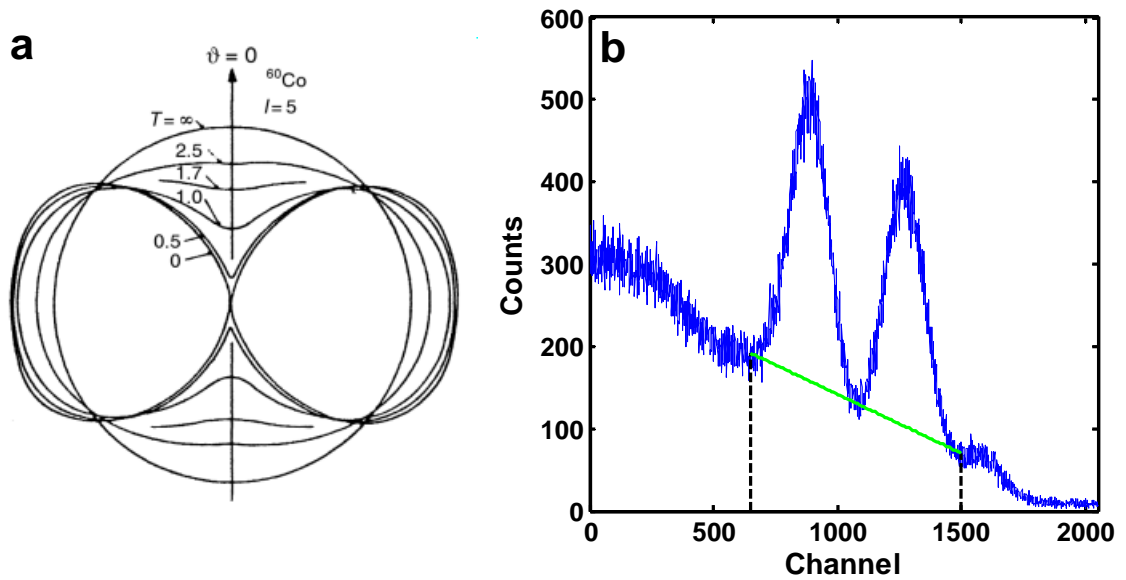


Figure A1: Nuclear orientation thermometry

(a) Angular radiation pattern of $^{60}\text{Co}^{98}$, (b) Example of gamma ray spectrum taken at 50 mK

Fig. A1a shows an example of the gamma ray pattern. The detection is done at the angle for which the change over temperature is maximum ($\vartheta = 0$). As shown in Fig. A1b, a multichannel analyzer is used to take gamma ray spectrum, and the integrated count number between the lower and upper energy limit (black dashed lines) with a subtraction of background (green line) is taken. Its ratio over the count at “hot” temperature (normally 4 K) gives the calibrated temperature.

A RuO₂ thermometer^{iv}, which is one of the matched pairs with one that is calibrated down to 50 mK, serves as the standard thermometer to 50mK. Other resistance thermometers are calibrated against this RuO₂ thermometer and used for monitoring various points in the dilution refrigerator. Between 18mK and 50mK, the temperature is calibrated against a nuclear orientation thermometer.

^{iv} manufactured by Lakeshore cryotronics Inc.

Appendix B

Mode shapes and resonance frequencies of a doubly-clamped beam

A small vibration of a beam can be described by Euler-Bernoulli equation. For a beam with thickness t (x -axis), width w (y -axis), and length l (z -axis), the equation of small deflection $X(z, t)$ in the x -axis is¹⁰⁰,

$$\rho S \ddot{X} = EI \frac{\partial^4 X}{\partial z^4}$$

where ρ is the density, S is the cross sectional area ($=wh$), E is the Young's modulus, and I is the moment of inertia about the y -axis ($=wh^3/12$). With the doubly-clamped boundary condition, $X(z=0, l) = dX/dz(z=0, l) = 0$, the harmonic solution yields mode shapes,

$$X_n(z) = A\{(\sin \kappa_n l - \sinh \kappa_n l)(\cos \kappa_n z - \cosh \kappa_n z) - (\cos \kappa_n l - \cosh \kappa_n l)(\sin \kappa_n z - \sinh \kappa_n z)\}$$

where κ_n is a root of $\cos \kappa_n l \cosh \kappa_n l = 1$ (e.g., $\kappa_n l = 4.73, 7.85, 11.00, \dots$)

and its eigenfrequencies,

$$\omega_n = \kappa_n^2 \sqrt{\frac{EI}{\rho S}}.$$

Appendix C

Coupled mode analysis of parametric amplification

Consider a driven, damped harmonic oscillator, with its spring constant modulated by

$k_p(t)$.

$$m\ddot{x} + \frac{m\omega_0}{Q}\dot{x} + (k + k_p(t))x = F(t) \quad (\text{Eq. C1})$$

Following a normal mode approach¹⁰¹, define complex amplitudes⁶⁴,

$$\begin{aligned} a &= \dot{x} + j\omega_1^* x \\ a^* &= \dot{x} - j\omega_1 x \end{aligned} \quad (\text{Eq. C2})$$

with $\omega_1 = \omega_0(\sqrt{1 - 1/4Q^2} + j/2Q) \cong \omega_0(1 + j/2Q)$ when $Q \gg 1$.

From Eqs. C1 and C2,

$$\begin{aligned} \frac{da}{dt} &= \ddot{x} + j\omega_1^* \dot{x} = (j\omega_1^* - \frac{\omega_0}{Q})\dot{x} - (k + k_p(t))\frac{x}{m} + \frac{F(t)}{m} \\ &\cong j\omega_1 a + j\frac{k_p(t)}{m} \frac{a - a^*}{\omega_1 + \omega_1^*} + \frac{F(t)}{m} \end{aligned} \quad (\text{Eq. C3})$$

Assume harmonic force, $F(t) = F_0 \cos(\omega_0 t + \varphi)$, and parametric modulation,

$k_p(t) = \Delta k \sin(2\omega_0 t)$. For a trial solution, a stationary state solution, $a = Ae^{j\omega_0 t}$, is

assumed, and collecting $e^{j\omega_0 t}$ gives,

$$j(\omega_1 - \omega_0)A - \frac{\Delta k}{2m(\omega_1 + \omega_1^*)} A^* + \frac{F_0}{2m} e^{j\varphi} \cong -\frac{\omega_0}{2Q} A - \frac{\Delta k}{4m\omega_0} A^* + \frac{F_0}{2m} e^{j\varphi} = 0 \quad (\text{Eq. C4})$$

$$\therefore A = \frac{F_0 Q}{m\omega_0} \left(\frac{\cos \varphi}{1 + Q\Delta k / 2k} + j \frac{\sin \varphi}{1 - Q\Delta k / 2k} \right) \quad (\text{Eq. C5}).$$

The parametric gain is,

$$\left| \frac{A}{A(\Delta k = 0)} \right| = \sqrt{\frac{\cos^2 \varphi}{(1 + Q\Delta k / 2k)^2} + \frac{\sin^2 \varphi}{(1 - Q\Delta k / 2k)^2}} \quad (\text{Eq. C6})$$

and for a small $\Delta k \cong 2k\delta\omega_0 / \omega_0$,

$$\left| \frac{A}{A(\delta\omega_0 = 0)} \right| = \sqrt{\frac{\cos^2 \varphi}{(1 + Q\delta\omega_0 / \omega_0)^2} + \frac{\sin^2 \varphi}{(1 - Q\delta\omega_0 / \omega_0)^2}}.$$

Appendix D

Driven responses of nanomechanical resonator

Driven responses of the nanomechanical resonator are measured using the combination of a red-detuned internal voltage $V_R \cos(\omega_R t) = V_R \cos((\omega_0 - \omega_m)t)$ and a sweeping voltage $V_S \cos(\omega_S t) = V_S \cos((\omega_0 + \delta)t)$. The force on the mechanical resonator around ω_m is given by,

$$F(\delta) = -\frac{1}{2} \frac{\partial C_g}{\partial x} V_R V_S \cos((\omega_m + \delta)t) \cong -4\hbar \frac{\partial \omega_0}{\partial x} \sqrt{n_p n_s}$$

where $n_{p,s} = (1/2)CV_{R,S}^2 / (\hbar\omega_0)$. With $n_p = 7 \cdot 10^4$, $n_s = 90$, $F = 1\text{fN}$, and the corresponding mechanical displacement is about 3 nm.

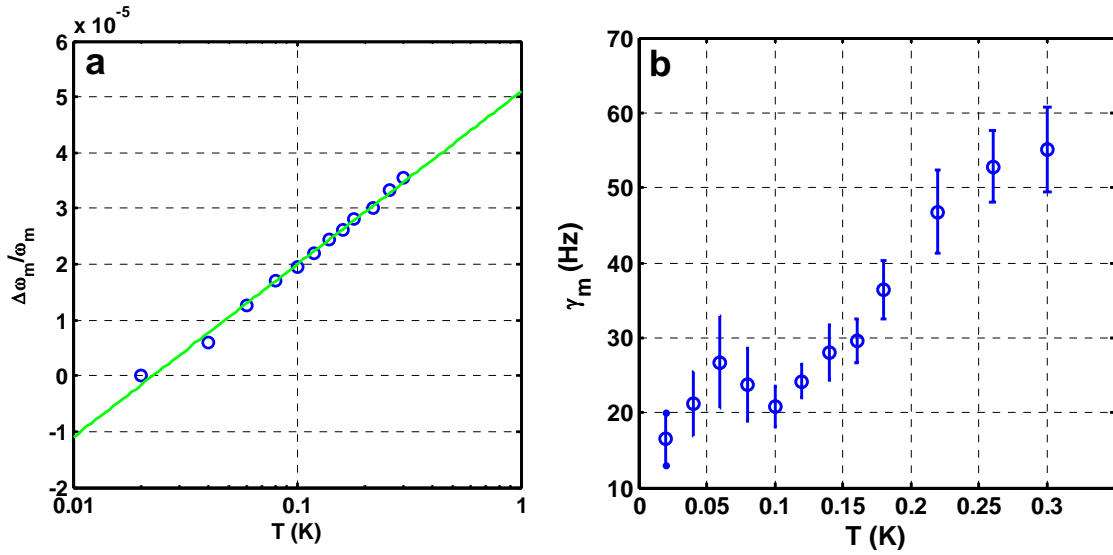


Figure D1: Driven response of nanomechanical resonator

(a) Fractional resonance frequency shift vs. temperature, (b) The linewidth of mechanical resonance vs. temperature

In Fig. D1, the fractional change of the resonance frequency shows logarithmic dependence on the temperature, and the damping is roughly $\sim T$. A broad peak around 50 mK in the damping data is visible, which is not clearly understood yet. For the resonance frequency shift data, a linear fit (green line) gives $\partial(\Delta\omega_m/\omega_m)/\partial(\ln(T)) = 1.3 \cdot 10^{-5}$.

Appendix E

Whispering gallery mode sapphire filter for microwave phase noise reduction

As discussed in Chapter 4, the back-action cooling limit is given by the occupation of the CPW resonator, provided there are no other sources of heating. Commercial microwave sources (e.g., Agilent E8257) have phase noise which can easily populate the CPW resonator more than 10 quanta at high microwave powers needed for the measurement. To filter out the phase noise, Rocheleau et. al.⁶⁶ used a LN2 cooled copper cavity. To improve the phase noise rejection and also to facilitate room-temperature operation, we developed a whispering gallery mode sapphire filter with a frequency stabilizing circuit. Dr. Matt Shaw and Steven Gutierrez designed and fabricated the circuit. 23 dB isolation was measured for 7.2 MHz detuning. This was enough to suppress the CPW occupation due to the phase noise down to 0.1 quanta.

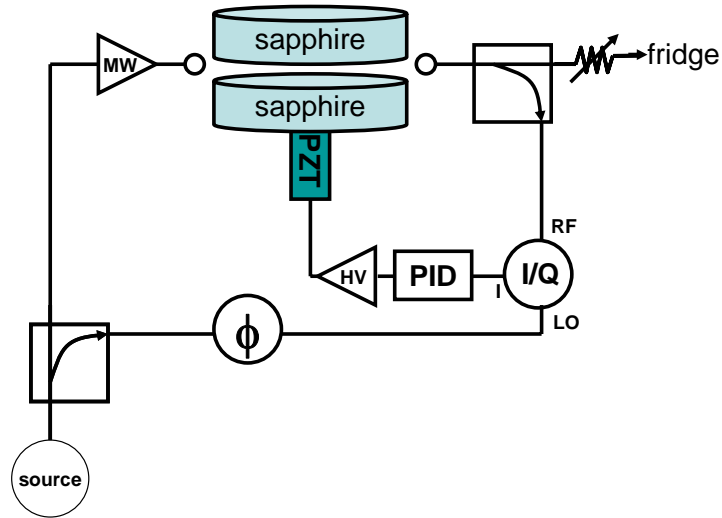


Figure E1: Schematic of the filter circuit

The mode frequency can be modulated by adjusting the gap between the two sapphire disks. For drift stabilization, it uses an I/Q mixer to extract the phase component of the filtered output, and then does PID feedback to stabilize it at the setpoint value.

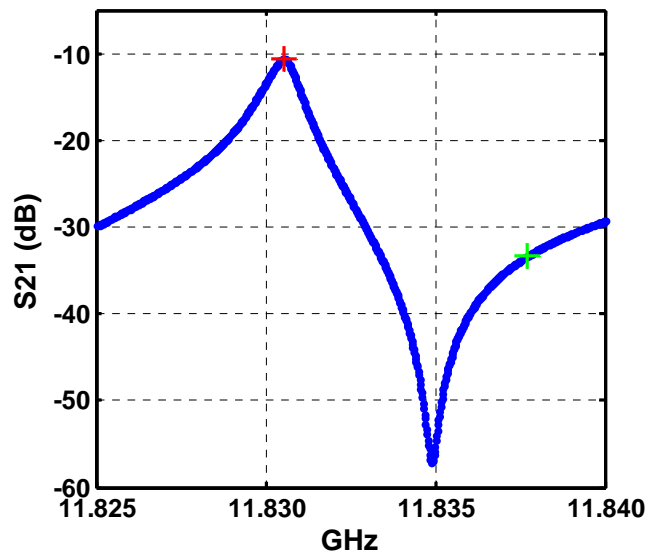


Figure E2: Transmission through the filter circuit

The red cross is where the red tone is located and the green cross is at the CPW resonance.

Bibliography

- ¹ H. Cavendish, *Phil. Trans. R. Soc. Lond.* **88**, 469 (1798).
- ² C.-A. d. Coulomb, *Histoire de l'Académie Royale des Sciences*, 569 (1785).
- ³ A. N. Cleland and M. L. Roukes, *Nature* **392**, 160 (1998).
- ⁴ D. Rugar, R. Budakian, H. J. Mamin, and B. W. Chui, *Nature* **430**, 329 (2004).
- ⁵ Y. T. Yang, C. Callegari, X. L. Feng, K. L. Ekinici, and M. L. Roukes, *Nano Lett.* **6**, 583 (2006).
- ⁶ K. Jensen, K. Kim, and A. Zettl, *Nat Nano* **3**, 533 (2008).
- ⁷ H.-Y. Chiu, P. Hung, H. W. C. Postma, and M. Bockrath, *Nano Lett.* **8**, 4342 (2008).
- ⁸ B. Abbott et. al., *Nucl. Instrum. Methods Phys. Res., Sect. A* **517**, 154 (2004).
- ⁹ C. M. Caves, K. S. Thorne, R. W. P. Drever, V. D. Sandberg, and M. Zimmermann, *Reviews of Modern Physics* **52**, 341 (1980).
- ¹⁰ X. M. Henry Huang, C. A. Zorman, M. Mehregany, and M. L. Roukes, *Nature* **421**, 496 (2003).
- ¹¹ A. D. O'Connell et. al., *Nature* **464**, 697 (2010).
- ¹² D. H. Santamore, A. C. Doherty, and M. C. Cross, *Phys. Rev. B* **70**, 144301

(2004).

- 13 M. D. LaHaye, O. Buu, B. Camarota, and K. C. Schwab, *Science* **304**, 74 (2004).
- 14 R. G. Knobel and A. N. Cleland, *Nature* **424**, 291 (2003).
- 15 A. Naik, O. Buu, M. D. LaHaye, A. D. Armour, A. A. Clerk, M. P. Blencowe, and
K. C. Schwab, *Nature* **443**, 193 (2006).
- 16 N. E. Flowers-Jacobs, D. R. Schmidt, and K. W. Lehnert, *Phys. Rev. Lett.* **98**,
096804 (2007).
- 17 A. N. Cleland, J. S. Aldridge, D. C. Driscoll, and A. C. Gossard, *Appl. Phys. Lett.*
81, 1699 (2002).
- 18 V. B. Braginsky and F. Y. Khalili, *Quantum measurement* (Cambridge, 1995).
- 19 Y. Nakamura, Y. A. Pashkin, and J. S. Tsai, *Nature* **398**, 786 (1999).
- 20 J. M. Martinis, S. Nam, J. Aumentado, and C. Urbina, *Phys. Rev. Lett.* **89**, 117901
(2002).
- 21 I. Chiorescu, Y. Nakamura, C. J. P. M. Harmans, and J. E. Mooij, *Science* **299**,
1869 (2003).
- 22 P. K. Day, H. G. LeDuc, B. A. Mazin, A. Vayonakis, and J. Zmuidzinas, *Nature*
425, 817 (2003).
- 23 E. K. Irish and K. Schwab, *Phys. Rev. B* **68**, 155311 (2003).

- 24 A. Wallraff, D. I. Schuster, A. Blais, L. Frunzio, R.-S. Huang, J. Majer, S. Kumar,
S. M. Girvin, and R. J. Schoelkopf, *Nature* **431**, 162 (2004).
- 25 A. A. Clerk, F. Marquardt, and K. Jacobs, *New J. Phys.* **10**, 095010 (2008).
- 26 A. D. Armour, M. P. Blencowe, and K. C. Schwab, *Phys. Rev. Lett.* **88**, 148301
(2002).
- 27 I. Martin, A. Shnirman, L. Tian, and P. Zoller, *Phys. Rev. B* **69**, 125339 (2004).
- 28 A. N. Cleland and M. R. Geller, *Phys. Rev. Lett.* **93**, 070501 (2004).
- 29 P. Rabl, A. Shnirman, and P. Zoller, *Phys. Rev. B* **70**, 205304 (2004).
- 30 L. Tian, *Phys. Rev. B* **72**, 195411 (2005).
- 31 E. Buks and M. P. Blencowe, *Phys. Rev. B* **74**, 174504 (2006).
- 32 L. F. Wei, Y.-x. Liu, C. P. Sun, and F. Nori, *Phys. Rev. Lett.* **97**, 237201 (2006).
- 33 K. Jacobs, P. Lougovski, and M. Blencowe, *Phys. Rev. Lett.* **98**, 147201 (2007).
- 34 A. A. Clerk and D. W. Utami, *Phys. Rev. A* **75**, 042302 (2007).
- 35 J. Hauss, A. Fedorov, C. Hutter, A. Shnirman, and G. Schön, *Phys. Rev. Lett.* **100**,
037003 (2008).
- 36 K. Jacobs, A. N. Jordan, and E. K. Irish, *EPL (Europhysics Letters)* **82**, 18003
(2008).
- 37 D. Wahyu Utami and A. A. Clerk, *Phys. Rev. A* **78**, 042323 (2008).

- 38 A. D. Armour and M. P. Blencowe, *New J. Phys.* **10**, 095004 (2008).
- 39 S. Haroche and J. M. Raimond, *Exploring the Quantum: Atoms, Cavities, and Photons* (Oxford Univ. Press, 2006).
- 40 Y. Makhlin, G. Schön, and A. Shnirman, *Reviews of Modern Physics* **73**, 357 (2001).
- 41 D. F. Walls and G. J. Milburn, *Quantum optics* (Springer, 1995).
- 42 D. V. Averin and C. Bruder, *Phys. Rev. Lett.* **91**, 057003 (2003).
- 43 M. A. Sillanpää, T. Lehtinen, A. Paila, Y. Makhlin, L. Roschier, and P. J. Hakonen, *Phys. Rev. Lett.* **95**, 206806 (2005).
- 44 T. Duty, G. Johansson, K. Bladh, D. Gunnarsson, C. Wilson, and P. Delsing, *Phys. Rev. Lett.* **95**, 206807 (2005).
- 45 T. A. Fulton and G. J. Dolan, *Phys. Rev. Lett.* **59**, 109 (1987).
- 46 J. M. Martinis, M. H. Devoret, and J. Clarke, *Phys. Rev. B* **35**, 4682 (1987).
- 47 P. A. Truitt, J. B. Hertzberg, C. C. Huang, K. L. Ekinci, and K. C. Schwab, *Nano Lett.* **7**, 120 (2007).
- 48 B. S. Palmer, C. A. Sanchez, A. Naik, M. A. Manheimer, J. F. Schneiderman, P. M. Echternach, and F. C. Wellstood, *Phys. Rev. B* **76**, 054501 (2007).
- 49 D. I. Schuster, *Circuit Quantum Electrodynamics*, Ph.D. thesis (Yale University,

2007).

- 50 M. Sillanpää, T. Lehtinen, A. Paila, Y. Makhlin, and P. Hakonen, *Phys. Rev. Lett.* **96**, 187002 (2006).
- 51 C. M. Wilson, T. Duty, F. Persson, M. Sandberg, G. Johansson, and P. Delsing, *Phys. Rev. Lett.* **98**, 257003 (2007).
- 52 D. I. Schuster et. al., *Nature* **445**, 515 (2007).
- 53 A. Heidmann, R. J. Horowicz, S. Reynaud, E. Giacobino, C. Fabre, and G. Camy, *Phys. Rev. Lett.* **59**, 2555 (1987).
- 54 A. La Porta, R. E. Slusher, and B. Yurke, *Phys. Rev. Lett.* **62**, 28 (1989).
- 55 R. M. Shelby, M. D. Levenson, S. H. Perlmutter, R. G. DeVoe, and D. F. Walls, *Phys. Rev. Lett.* **57**, 691 (1986).
- 56 R. E. Slusher, L. W. Hollberg, B. Yurke, J. C. Mertz, and J. F. Valley, *Phys. Rev. Lett.* **55**, 2409 (1985).
- 57 L.-A. Wu, H. J. Kimble, J. L. Hall, and H. Wu, *Phys. Rev. Lett.* **57**, 2520 (1986).
- 58 M. A. Castellanos-Beltran, K. D. Irwin, G. C. Hilton, L. R. Vale, and K. W. Lehnert, *Nature Phys.* **4**, 929 (2008).
- 59 R. Movshovich, B. Yurke, P. G. Kaminsky, A. D. Smith, A. H. Silver, R. W. Simon, and M. V. Schneider, *Phys. Rev. Lett.* **65**, 1419 (1990).

- 60 B. Yurke, P. G. Kaminsky, R. E. Miller, E. A. Whittaker, A. D. Smith, A. H. Silver,
and R. W. Simon, *Phys. Rev. Lett.* **60**, 764 (1988).
- 61 A. Dana, F. Ho, and Y. Yamamoto, *Appl. Phys. Lett.* **72**, 1152 (1998).
- 62 R. B. Karabalin, X. L. Feng, and M. L. Roukes, *Nano Lett.* **9**, 3116 (2009).
- 63 I. Mahboob and H. Yamaguchi, *Appl. Phys. Lett.* **92**, 173109 (2008).
- 64 D. Rugar and P. Grüter, *Phys. Rev. Lett.* **67**, 699 (1991).
- 65 M. P. Blencowe and M. N. Wybourne, *Physica B* **280**, 555 (2000).
- 66 T. Rocheleau, T. Ndukum, C. Macklin, J. B. Hertzberg, A. A. Clerk, and K. C.
Schwab, *Nature* **463**, 72 (2010).
- 67 A. N. Cleland, *Foundations of Nanomechanics* (Springer, 2003).
- 68 C. M. Caves, *Phys. Rev. D* **26**, 1817 (1982).
- 69 A. A. Clerk, *Phys. Rev. B* **70**, 245306 (2004).
- 70 K. Jacobs, *Phys. Rev. Lett.* **99**, 117203 (2007).
- 71 F. L. Semião, K. Furuya, and G. J. Milburn, *Phys. Rev. A* **79**, 063811 (2009).
- 72 M. D. LaHaye, J. Suh, P. M. Echternach, K. C. Schwab, and M. L. Roukes,
Nature **459**, 960 (2009).
- 73 R. Lifshitz and M. C. Cross, *Reviews of Nonlinear Dynamics and Complexity*
(Wiley-VCH, 2008).

- 74 R. Lifshitz and M. C. Cross, Phys. Rev. B **67**, 134302 (2003).
- 75 S. Zaitsev, O. Shtempluck, E. Buks, and O. Gottlieb, arXiv:0911.0833 (2009).
- 76 R. Almog, S. Zaitsev, O. Shtempluck, and E. Buks, Phys. Rev. Lett. **98**, 078103
(2007).
- 77 B. Yurke and E. Buks, J. Lightwave Technol. **24**, 5054 (2006).
- 78 K. Wodkiewicz, B. W. Shore, and J. H. Eberly, Phys. Rev. A **30**, 2390 (1984).
- 79 H. Rothe and W. Dahlke, Proc. IRE **44**, 811 (1956).
- 80 M. Hofheinz et. al., Nature **454**, 310 (2008).
- 81 F. Marquardt, J. P. Chen, A. A. Clerk, and S. M. Girvin, Phys. Rev. Lett. **99**,
093902 (2007).
- 82 I. Wilson-Rae, N. Nooshi, W. Zwerger, and T. J. Kippenberg, Phys. Rev. Lett. **99**,
093901 (2007).
- 83 A. Schliesser, O. Arcizet, R. Riviere, G. Anetsberger, and T. J. Kippenberg, Nat
Phys **5**, 509 (2009).
- 84 Y.-S. Park and H. Wang, Nat Phys **5**, 489 (2009).
- 85 S. Groblacher, J. B. Hertzberg, M. R. Vanner, G. D. Cole, S. Gigan, K. C. Schwab,
and M. Aspelmeyer, Nat Phys **5**, 485 (2009).
- 86 J. D. Teufel, J. W. Harlow, C. A. Regal, and K. W. Lehnert, Phys. Rev. Lett. **101**,

197203 (2008).

- 87 D. M. Pozar, *Microwave Engineering* (Wiley, 2005).
- 88 F. Marquardt, A. A. Clerk, and S. M. Girvin, *Journal of Modern Optics* **55**, 3329 (2008).
- 89 J. B. Hertzberg, *Back-action evading measurements of nanomechanical motion approaching quantum limits*, Ph.D. thesis (University of Maryland, 2009).
- 90 J. Gao, *The Physics of Superconducting Microwave Resonators*, Ph.D. thesis (California Institute of Technology, 2008).
- 91 J. Gao, J. Zmuidzinas, B. A. Mazin, H. G. LeDuc, and P. K. Day, *Appl. Phys. Lett.* **90**, 102507 (2007).
- 92 W. A. Phillips, *Rep. Prog. Phys.* **50**, 1657 (1987).
- 93 S. Hunklinger, W. Arnold, and S. Stein, *Phys. Lett. A* **45**, 311 (1973).
- 94 R. N. Kleiman, G. Agnolet, and D. J. Bishop, *Phys. Rev. Lett.* **59**, 2079 (1987).
- 95 L. Piché, R. Maynard, S. Hunklinger, and J. Jäckle, *Phys. Rev. Lett.* **32**, 1426 (1974).
- 96 B. Golding and J. E. Graebner, in *Amorphous solids*, edited by W. A. Phillips (Springer-Verlag, 1981).
- 97 J. Yang, T. Ono, and M. Esashi, *Appl. Phys. Lett.* **77**, 3860 (2000).

- ⁹⁸ F. Pobell, *Matter and methods at low temperatures* (Springer, 1995).
- ⁹⁹ H. Marshak, *Journal of Research of the National Bureau of Standards* **88**, 175 (1983).
- ¹⁰⁰ L. D. Landau, L. P. Pitaevskii, E. M. Lifshitz, and A. M. Kosevich, *Theory of Elasticity* (Elsevier, 1986).
- ¹⁰¹ W. H. Louisell, *Coupled mode and parametric electronics* (John Wiley & Sons, 1960).